Generated using the official AMS LaTeX template v5.0

A data assimilation approach to last millennium temperature field reconstruction using a limited high-sensitivity proxy network

Jonathan M. King*

Department of Geosciences and Laboratory of Tree-Ring Research, University of Arizona, Tucson, Arizona

Kevin J. Anchukaitis

School of Geography, Development, and Environment and Laboratory of Tree-Ring Research, University of Arizona, Tucson, Arizona

Jessica E. Tierney

Department of Geosciences, University of Arizona, Tucson, Arizona

Gregory J. Hakim

Department of Atmospheric Sciences, University of Washington, Seattle, Washington

Julien Emile-Geay and Feng Zhu

Department of Earth Sciences, University of Southern California, Los Angeles, California

Rob Wilson

School of Earth and Environmental Sciences, University of St Andrews, St Andrews, UK

**Corresponding author*: Jonathan King, jonking93@email.arizona.edu

ABSTRACT

Paleoclimate field reconstructions using data assimilation commonly employ large proxy networks, which are often composed of records that have a complex range of sensitivities to the target climate field. This can introduce biases into reconstructions or decrease overall skill. Smaller networks of highly-sensitive proxies provide an alternative, but have not been extensively used for assimilation and their strengths and limitations are less well understood. Here, we reconstruct Northern Hemisphere summer temperature anomalies over the last millennium by assimilating the NTREND network, a spatially and temporally limited collection of highly temperature-sensitive tree-ring records. Pseudo-proxy experiments indicate that the reconstruction can be sensitive to biases in the climate model prior, so we perform 10 assimilations each using a different model prior. Reconstructed temperature anomalies are most sensitive to prior selection when the network becomes sparse in space and time, but show greater consistency as the network grows. The method also underestimates temporal variability with a reduced network or in regions distal to the proxies. The effects of network attrition emphasize the importance of analyzing temperature anomalies in conjunction with reconstruction uncertainty, which emerges naturally for spatial fields from our ensemble method. A comparison of our reconstruction and five existing paleo-temperature products reveals large differences in the spatial patterns and magnitudes of reconstructed temperature anomalies in response to radiative forcing. These extant uncertainties call for development of a renewed paleoclimate reconstruction intercomparison framework for systematically examining the consequences of network composition and reconstruction methodological choices, as well as for expanded collection of new, longer, and highly-sensitive proxy data.

1. Introduction

Past variations in surface temperatures can be used to investigate a number of key characteristics of the Earth's climate system, including the response to radiative forcing, the regional effects of such forcings, and the role of internal modes of coupled ocean-atmosphere variability (Hegerl et al. 1997; Stott and Tett 1998; Delworth and Mann 2000; Meehl et al. 2004; Lean and Rind 2008; Stott and Jones 2009; Stott et al. 2010; Solomon et al. 2011; Phipps et al. 2013; Hegerl and Stott 2014; Kaufman 2014). Paleoclimate temperature reconstructions using natural archives like tree-rings, corals, speleothems and other 'proxies' are particularly useful because they extend the short instrumental record to centennial and longer timescales. These provide an opportunity to evaluate and characterize the magnitude and temporal patterns of forced and unforced climate response (Hegerl et al. 2003, 2007; Schurer et al. 2013; Masson-Delmotte et al. 2013). Spatial climate field reconstructions (CFRs) provide additional insight because they capture the details of regional climate variability and reveal the spatial fingerprints of large-scale temperature anomalies caused by radiative forcing and ocean-atmosphere dynamics (Mann et al. 1998; Evans et al. 2001; Seager et al. 2007; Cook et al. 2010a,b; Phipps et al. 2013; Anchukaitis and McKay 2015; Goosse 2017). CFRs have been developed using a number of methods (Tingley et al. 2012; Smerdon and Pollack 2016) including point-by-point methods (Cook et al. 1999, 2010a,b; Anchukaitis et al. 2017), several variants of regularized expectation maximization (RegEM; Schneider 2001; Rutherford et al. 2003; Mann et al. 2009; Smerdon et al. 2011; Guillot et al. 2015), and reduced space approaches (Fritts 1991; Cook et al. 1994; Mann et al. 1998; Evans et al. 2002; Gill et al. 2016).

Recently, data assimilation (DA) has emerged as a promising CFR technique (e.g. Widmann et al. 2010; Bhend et al. 2012; Goosse et al. 2012; Steiger et al. 2014; Hakim et al. 2016; Matsikaris et al. 2015; Okazaki and Yoshimura 2017; Steiger et al. 2018; Franke et al. 2020). Assimilation methods integrate the climate signals recorded in paleoclimate proxies with dynamical constraints provided by climate models. In doing so, they combine the strengths of both information sources. For example, paleoclimate simulations using transient boundary conditions capture the climate system's response to past forcing events in a physically consistent framework (Braconnot et al. 2012; Otto-Bliesner et al. 2016). The temporal evolution and spatial patterns of these simulated climates also reflect internal climate variability (Tebaldi et al. 2011; Deser et al. 2010) and therefore any paleoclimate simulation represents a single member from an ensemble of plausible climate trajectories, rather than the actual history of the Earth's climate system. In contrast, paleoclimate proxies reflect the actual historical climate state but are sparsely distributed, integrate climate variability across a range of timescales, and incorporate additional and potentially confounding non-climate information. Amongst other challenges, these characteristics hinder the reconstruction of distal climate fields and variables not directly sensed by the proxies (Hughes and Ammann 2009). By leveraging proxy records to constrain physically-consistent climate simulations, DA integrates observations and dynamics to produce full-field climate reconstructions and associated estimates of uncertainty that reflect the historical trajectory of the climate system.

There are several existing paleoclimate DA paradigms, including pattern nudging / forcing singular vectors (Van der Schrier and Barkmeijer 2005), particle filters (Goosse et al. 2012; Dubinkina and Goosse 2013; Matsikaris et al. 2015), and ensemble Kalman filters (Bhend et al. 2012; Steiger et al. 2014; Hakim et al. 2016; Dee et al. 2016; Perkins and Hakim 2017; Steiger et al. 2018; Tardif et al. 2019; Franke et al. 2020). Here, we focus on the ensemble Kalman filter (EnKF) approach (Steiger et al. 2014; Hakim et al. 2016), which has been shown to perform well compared to other DA methods (Liu et al. 2017). EnKF methods update an ensemble of climate states to more closely match paleoclimate proxy records. These climate states are produced using one of several approaches: the “online” method, in which the ensemble is generated by a set of evolving model simulations that propagate updates forward through time (e.g. Perkins and Hakim 2017); the “offline” (or “no-cycling”) method (Oke et al. 2002; Evensen 2003), in which a single, time-independent ensemble is constructed from pre-existing climate model output (e.g. Bhend et al. 2012; Annan and Hargreaves 2012; Steiger et al. 2014; Hakim et al. 2016; Tardif et al. 2019); or a hybrid of the two (e.g. Valler et al. 2019; Franke et al. 2020). We focus here on the offline approach, which has been shown to perform favorably to online methods with reduced computational costs (Matsikaris et al. 2015; Acevedo et al. 2017). A key requirement of EnKF methods is the ability to estimate proxy values from climate model output, which is achieved through the use of proxy-system models (PSMs; Evans et al. 2013). PSMs are forward models that translate climate state variables, such as temperature and precipitation, into proxy values, like tree-ring width (TRW) or maximum latewood density (MXD). PSMs can incorporate scientific understanding of the processes that transform climate signals to proxy records within a reconstruction (Hughes and Ammann 2009; Evans et al. 2013; Dee et al. 2015) and support separation of data and process level models in the data assimilation framework (Goosse 2016).

An important decision in any assimilation is the selection of the proxy network. Ultimately, this choice must balance spatiotemporal coverage with sensitivity to the reconstructed field (Esper et al. 2005; Frank et al. 2010; Wang et al. 2015; Wilson et al. 2016; Anchukaitis et al. 2017; Esper et al. 2018; Franke et al. 2020). In general, large networks maximize coverage, but their size often results from the inclusion of proxy records with comparatively weak, complex, or multivariate sensitivity to reconstructed variables. By contrast, smaller curated networks consisting of well-understood and strongly-sensitive proxies provide a higher ratio of signal to noise at the cost of reduced coverage (Frank et al. 2010). An additional consideration concerns PSM implementation: highly sensitive networks with a known climate response and seasonal window facilitate physically realistic PSMs, potentially improving assimilation skill. Given the complexity of these trade-offs, network selection is not necessarily intuitive. Noisy proxies that covary poorly with climate fields are down-weighted by the Kalman filter algorithm; if this down-weighting renders the effects of climate-insensitive proxies negligible on a reconstruction, then a large network incorporating many potentially proxies might appear preferable. However, work by Franke et al. (2020) indicates that EnKF temperature reconstructions using large proxy networks do not correlate with target temperatures as well as reconstructions produced using smaller, more sensitive networks. This result is supported by Tardif et al. (2019), who found that additional screening of proxy records for temperature sensitivity in an assimilation framework improved their ability to reconstruct salient pre-industrial climate features, such as cooling during the Little Ice Age. The importance of proxy sensitivity is further highlighted by Steiger and Smerdon (2017) who note that skillful hydroclimate DA requires proxies sensitive to the target reconstruction field.

Among the potential choices of curated temperature sensitive proxy networks for data assimilation include the PAGES2k (PAGES2k Consortium 2013, 2017) and NTREND networks (Wilson et al. 2016; Anchukaitis et al. 2017). The PAGES2k network is now commonly used in paleo-DA applications (Hakim et al. 2016; Dee et al. 2016; Okazaki and Yoshimura 2017; Perkins and Hakim 2017; Tardif et al. 2019; Neukom et al. 2019) and consists of proxy records identified as temperature-sensitive and meeting minimum temporal coverage and age model precision criteria during the Common Era (PAGES2k Consortium 2017). DA reconstructions using this network may implement additional statistical screening of the full proxy network but usually incorporate several hundred proxy records. The NTREND network has stricter requirements for inclusion: it consists of 54 published tree-ring chronologies and temperature reconstructions selected by dendroclimatologists that demonstrate an established and biophysically reasonable association with local seasonal temperatures(Wilson et al. 2016). Franke et al. (2020) proposed that the additional coverage of the PAGES2k network is preferable to the increased sensitivity of the smaller NTREND network for global and hemisphere-scale temperature reconstructions but found the NTREND network provided the best reconstruction in the extratropical Northern Hemisphere. To produce a maximally skillful reconstruction for this region, we focus on assimilating the NTREND network but acknowledge that this choice is accompanied by a reduced spatial extent.

Before performing an assimilation, we seek to understand the advantages and tradeoffs of offline EnKF related to both the proxy data and climate model priors. We undertake this investigation using pseudo-proxy experiments (Mann and Rutherford 2002; Zorita et al. 2003; Smerdon 2012), which allow us to test the method's ability to reconstruct climate fields within a controlled setting where the answer is known. Here, we note the importance of model selection in DA pseudo-proxy experiments and distinguish between "perfect-model" and "biased-model" experimental designs. In a perfect-model experiment, the Kalman filter uses the same model to generate both the target field and as the model prior. Such designs are common in DA analyses (Annan and Hargreaves 2012; Steiger et al. 2014; Okazaki and Yoshimura 2017; Acevedo et al. 2017; Zhu et al. 2020), where they are powerful tools for testing sensitivity to variables like proxy noise, network distribution, and calibration intervals. Biased-model paradigms use different climate models to generate target fields and assimilated model priors and thus can examine the effects of model spatial covariance and mean state biases. Dee et al. (2016) found model biases a potentially major source of error in paleo-EnKF reconstructions, so we employ both perfect and biased-model experiments in our investigations.

In this study, we assimilate the NTREND network to reconstruct May through August (MJJA) mean temperature anomalies (Wilson et al. 2016; Anchukaitis et al. 2017). Before performing this assimilation, we first evaluate the sensitivity of our method to proxy noise, network attrition, and climate model biases in a suite of pseudo-proxy experiments. We also use the pseudo-proxy framework to compare the skill of our data assimilation method to point-by-point regression (PPR), the reconstruction technique used for the original NTREND temperature field reconstruction (Anchukaitis et al. 2017). We then produce an ensemble of real reconstructions by assimilating the NTREND network with output from multiple models from the Coupled Modeling Intercomparison Project Phase 5 (CMIP5; Taylor et al. 2012) and the Community Earth System Model (CESM) Last Millennium Ensemble (LME; Otto-Bliesner et al. 2016). We quantify the skill of the DA reconstructions using spatial temperature anomaly fields, mean extratropical (30°N–90°N) May through August time series, and withheld proxy data. Finally, we examine the climate response of the ensemble mean reconstruction to radiative forcings and compare these responses to the results from previous temperature field reconstructions.

2. Methods

a. Proxy Network

The NTREND network is a curated set of 54 published annual resolution tree-ring based summer-temperature proxy records and temperature reconstructions (Figure 1; Wilson et al. 2016; Anchukaitis et al. 2017). The records are selected from published tree-ring chronologies or reconstructions, leveraging expert knowledge of each site to derive robust past temperature estimates. The collection was selected to maximize boreal summer temperature sensitivity while minimizing the response to other climate variables. While tree growth at the NTREND sites is primarily limited by summer growing temperatures, the optimal summer season varies between sites. Wilson et al. (2016) determined the season of highest temperature sensitivity for each site and identified mean MJJA temperatures anomalies as the optimal reconstruction target for the network as a whole. The network only includes sites between 40°N and 75°N as lower latitude trees tend to exhibit sensitivity to multiple climate influences, especially moisture limitations. Each record is derived from ring-width measurements (TRW), maximum latewood density (MXD; Schweingruber et al. 1978), or a mixture of TRW, MXD, and blue intensity (BI; McCarroll et al. 2002; Björklund et al. 2014; Rydval et al. 2014; Wilson et al. 2019). The network extends from 750 - 2011 CE, with maximum coverage over the period from 1710-1988 CE. Spatial coverage is greater over Eurasia (39 sites) than North America (15 sites), with a distinct spatial imbalance prior to 1000 CE (20 vs. 3). We end all reconstructions in 1988 CE as network attrition limits the utility of assimilated NTREND reconstructions after this point (Anchukaitis et al. 2017).

b. Data Assimilation

Our data assimilation method uses an ensemble Kalman filter (EnKF) approach (Evensen 1994; Steiger et al. 2014) to update an initial ensemble of climate states ($\mathbf{X_p}$) given proxy data ($\mathbf{Y}$) in each reconstructed annual time step. We use an EnKF variant known as the ensemble square root Kalman filter (EnSRF; Andrews 1968), with an "offline" (or "no-cycling") approach (Oke et al. 2002; Evensen 2003). Unlike several similar implementations (e.g. Steiger et al. 2014; Hakim et al. 2016; Tardif et al. 2019), we do not use a serial update scheme and do not append mean fields to end of the state vector. The complete details of our approach are given in the Appendix. The Kalman Filter can be expressed as a recursive Bayesian filter (Chen et al. 2003; Wikle and Berliner 2007) wherein new information ($\mathbf{Y}$) is used to update estimates of state parameters ($\mathbf{X}$). Hence, we will often refer to $\mathbf{X_p}$ and the updated ensemble ($\mathbf{X_a}$ as the model prior and posterior.

We construct prior ensembles using output from the past1000 and historical experiments of the Coupled Modeling Intercomparison Project Phase 5 (CMIP5; Taylor et al. 2012) as well as the Last Millennium Ensemble (LME; Otto-Bliesner et al. 2016). For a given assimilation, we use values from a single climate model and designate each year of available output as a unique ensemble member. A summary of the model ensembles is given in Table 1. All CMIP5 data are for the r1i1p1 configuration, and LME output was selected from full-forcing run 2. To avoid the effects of climate model mean state biases, we assimilate temperature anomalies. All values in the prior are determined by subtracting the 1951-1980 CE mean temperature from the corresponding values in the model output.

In each assimilation, model estimates of values for the j^{th} proxy record are determined by applying a corresponding PSM to the prior ensemble. Following a similar methodology as Tardif et al. (2019), we use linear, univariate PSMs trained on the mean temperature of the optimal growing season unique to each site (Wilson et al. 2016), such that:

$$\mathbf{y}_{\mathbf{e}_j} = \text{PSM}_j(\mathbf{X_p}) = \alpha_j + \beta_j \mathbf{T}_j \tag{1}$$

where ($\mathbf{y}_{\mathbf{e}_j}$) is a vector of model estimates, and $\mathbf{T}_j$ is a vector of mean growing season temperature anomalies from the climate model grid point closest to the proxy site. We determine the coefficients α_j and β_j by regressing the corresponding NTREND record against its mean growing season temperature anomaly at the closest land grid cell in CRU-TS 4.01 (Harris et al. 2014). We perform the regression using all overlapping years, and the intercept and slope are used respectively as α_j and β_j. The variances of the regression residuals are used as the observation uncertainties and these values range from 0.23 to 1.34 in proxy units.

We implement a covariance localization scheme, which limits the influence of proxies outside of a specified radius, a procedure somewhat analogous to the search radii used in PPR. Localization was originally developed to limit spurious covariance arising from sampling noise in small ensembles of $m \leq 50$ (Houtekamer and Mitchell 2001). Our offline approach enables the use of much larger ensembles ($m > 1000$), but we note that spurious covariances may still arise from biases in a climate model's covariance structure. Consequently, for paleoclimate applications, localization can improve the quality of assimilated reconstructions even for large prior ensembles. The localization radius is an important free parameter in this method and must be assessed independently for different model priors, reconstruction targets, and proxy networks. The process used to select localization radii for these experiments is detailed in the Appendix and the selected radii are summarized in Tables 2 and S1.

In total, we perform 10 DA reconstructions, each using a different model prior (Table 1). In all reconstructions, we update the mean May through August (MJJA) temperature anomaly field, rather than individual months. We assess the skill of each assimilation by examining the Pearson's correlation coefficients, root mean square error (RMSE), mean biases, and standard deviation ratios (c.f. Smerdon et al. 2011):

$$\sigma_{\text{ratio}} = \frac{\sigma_{\text{reconstruction}}}{\sigma_{\text{target}}} \tag{2}$$

of various reconstructed time series relative to targets. Specifically, we validate using mean extratropical (30°N–90°N) MJJA time series, instrumental spatial field grid point time series, and independent proxy record time series. The skill of the extratropical time series is determined using a Monte Carlo of calibration and validation periods detailed in the Appendix. Spatial skill is computed against the Berkeley Earth surface temperature field (BE; Rohde et al. 2013) over the period 1901 - 1988 CE. We note that the BE instrumental record is not used in the PSM and localization calibrations, which instead leverage the CRU product. To assess the ability of DA to reconstruct withheld proxy time series, we perform a series of leave-one-out assimilations for each model by iteratively removing a single proxy time-series from the NTREND network and re-running the assimilation using the remaining 53 records. We next produce an estimate of the removed proxy by applying Equation 1 to the reconstruction and assess skill metrics for this estimated proxy record. We note that we update the temperature anomalies for the site's optimal growing season, rather than MJJA, to enable the use of Equation (1). We iterate this procedure over the full NTREND network, which produces independent proxy verification metrics for each record.

We next determine the ensemble-mean of the extratropical MJJA time series across all 10 DA reconstructions and quantify both the uncertainty resulting from the choice of model prior and the 2σ width of the posterior ensembles. Here, σ is the standard deviation of temperature anomalies across the posterior ensemble. We compare the ensemble-mean extratropical time series to the analogous time series extracted from the Anchukaitis et al. (2017) PPR reconstruction. We then produce an ensemble-mean spatial reconstruction by linearly interpolating each reconstruction to the lowest model resolution and averaging. We obtain posterior ensemble uncertainty estimates for this ensemble-mean reconstruction by taking the square root of the sum of the posterior variances for the 10 reconstructions and dividing by 10. We compare this ensemble-mean product to several recent temperature CFRs, which are summarized in Table 3. In brief, Guillet et al. (2017) focused on reconstructing high-frequency temperature anomalies associated with known volcanic eruptions using a network of a similar size and composition to the NTREND network in a linear regression framework and their work provides a comparison point with Anchukaitis et al. (2017). The LMR 2.1 reconstruction applied an offline EnSRF DA to the PAGES2k network and allows us to compare DA reconstructions using different proxy networks (Tardif et al. 2019). From Zhu et al. (2020), we examine the reconstruction of mean June through August (JJA) temperatures using PAGES2k trees. The Neukom et al. (2019) DA offers another comparison point, using a proxy network of intermediate size derived from a screened version of PAGES2k. Neukom et al. (2019) performed an ensemble of reconstructions using different methods and recommend using the ensemble mean reconstruction for climate analysis; however, we only focus on the DA product to emphasize the differences in reconstructions that arise even when using similar methodologies.

c. *Pseudo-proxy Experiments*

Before assimilating the real NTREND network, we first examine the skill of our DA method in a pseudo-proxy framework (Smerdon 2012). This approach allows us to test the method's ability to reconstruct known climate field targets within a controlled setting. Here, we specify the target fields as surface temperatures from the years 850-2005 CE from either the Last Millennium Ensemble full-forcing run 2 (CESM; Otto-Bliesner et al. 2016), or from the combined last millennium and historical runs of the Max Planck Institute for Meteorology Earth System Model (MPI; Marsland et al. 2003; Stevens et al. 2013). While this experimental design is intentionally tractable, we caution that the specific spatial patterns of skill in these experiments will depend on the specific models used (Smerdon et al. 2011), but also note that the framework allows us to test the sensitivity of the DA method as a whole. Here, we are interested in examining the sensitivity of EnSRF to the proxy network and climate model prior, so we systematically explore the effects of noisy proxy records, network attrition, and biased climate models on DA performance.

In each experiment, we generate pseudo-proxies by applying the PSMs from Equation 1 to the target climate model field. The pseudo-proxies therefore mimic the temperature response of the real NTREND network. We examine the effects of proxy noise by selectively neglecting or adding Gaussian white noise to the pseudo-proxies, such that:

$$\hat{\mathbf{y}}_j = \alpha_j + \beta_j \mathbf{T}_j^{\text{target}} + \epsilon_j \tag{3}$$

$$\epsilon_j \sim \begin{cases} 0, & \text{Perfect} \\ \mathcal{N}(0, \mathrm{R_{jj}}), & \text{Noisy} \end{cases} \tag{4}$$

where $\hat{\mathbf{y}}_j$ is the j^{th} pseudo-proxy record, $\mathbf{T}_j^{\text{target}}$ is the vector of mean growing season temperature anomalies from the grid cell closest to the proxy site in the target climate field, and R_{jj} is the j^{th} diagonal element of $\mathbf{R}$.

After generating the pseudo-proxies for a given experiment, we next design a set of PSMs for the pseudo-proxy reconstructions by mirroring the process used to design the PSMs in Equation 1. Rather than regressing the real NTREND network against CRU-TS 4.01, we instead regress the pseudo-proxies against the target climate model field. We use the same set of overlapping years as in the NTREND/CRU-TS 4.01 regression to most closely mimic the real calibration procedure. Note that noise added to the pseudo-proxies will affect the statistics obtained from the pseudo-proxy/target-field regressions. Consequently, model estimates for the pseudo-proxies are given by:

$$\hat{\mathbf{y}}_{\mathbf{e}_j} = \widehat{\mathrm{PSM}}_j(\mathbf{X_p}) = \hat{\alpha}_j + \hat{\beta}_j \mathbf{T}_j \tag{5}$$

where $\hat{\alpha}_j$ and $\hat{\beta}_j$ are estimates of the α_j and β_j used to generate a given pseudo-proxy record. This mimics how proxy-noise and sampling errors can introduce errors into PSMs calibrated on real data. After generating pseudo-proxy model estimates we next select a climate model to use as the prior ensemble for the data assimilation. Localization radii for each pseudo-proxy assimilation are detailed in Table S1. We test each combination of target field and model prior for LME and MPI, which allows us to alternate between perfect-model and biased-model experimental designs. For each target-prior pair, we alternatively assimilate the full set of pseudo-proxies and pseudo-proxies displaying realistic temporal attrition. Finally, we produce an analogous set of pseudo-proxy reconstructions using point-by-point regression (PPR) and compare their skill to the DA reconstructions.

d. Point-by-point Regression

PPR is a "region of interest" CFR technique that calculates a nested multivariate regression model between predictor network and a target field (Cook et al. 1999). The method was motivated by the premise that proxies near a reconstructed grid point are more likely to be true records of climate at that site. Consequently, PPR uses a strict search radius to select proxy predictor series for each grid point reconstruction. The method was originally used for drought reconstructions (Cook et al. 1999, 2010a,b), but was later adapted by Cook et al. (2013) to reconstruct continental temperature anomalies. Anchukaitis et al. (2017) further adapted the method to reconstruct hemispheric temperature anomalies and we follow their implementation in this study.

In brief, given a target of gridded climate observation, the method first identifies proxy sites within 1000 km of each grid point centroid. If no proxy records are found within 1000 km, the search radius is expanded in 500 km increments to a maximum of 2000 km to find predictor sites. These radii are based on decorrelation decay lengths in the observational temperature field from Cowtan and Way (2014). If no predictors are found within 2000 km, then no reconstruction is performed for the grid. A multivariate regression model is then calibrated against the MJJA temperature values of the target field Cowtan and Way (2014) for each grid point over the period 1945 to 1988 CE, and the reconstructions are validated using withheld temperature data for the period 1901 to 1944 CE. As the number of records declines back through time, the regression model is recalibrated and validated for each change in network size (Meko 1997; Cook et al. 1999). For a given grid point, temperature anomalies are obtained for all years in which at least one predictor record remains within the initial search radius. Following Anchukaitis et al. (2017), we then screen the final reconstructed field in each time step to only include grid cells where the reduction of error

(RE) statistic is greater than zero and where the reconstruction extends to at least 1000 CE. RE is defined at each grid point as (c.f. Cook et al. 1999; Wilson et al. 2006):

$$RE = 1 - \frac{\Sigma(x_v - \hat{x}_v)^2}{\Sigma(x_c - \bar{x}_c)^2} \tag{6}$$

where x_v and $\hat{x}_v$ are observed and reconstructed temperatures during the validation interval, and x_c and $\bar{x}_c$ are observed temperatures and their mean during the calibration interval. We use this screened field as the final spatial MJJA temperature reconstruction and also use this screened product to determine mean extratropical MJJA time series.

3. Results

a. Pseudo-proxy experiments

Figure 2 shows the spatial correlations of the NTREND DA pseudo-proxy temperature reconstructions relative to their target fields. The pseudo-proxy reconstructions are most skillful in the extratropical Northern Hemisphere with correlations greater than 0.9 near the proxy sites. Correlations are lower over ocean basins and with increasing distance from the proxy network. All reconstructions show reduced correlations over the Southern Hemisphere, with slightly negative value in the high-latitudes of the biased-model experiments. Network attrition and proxy noise cause comparatively minor reductions in reconstruction correlations and have little effect on the broad spatial fingerprints. By comparison, in these experiments the climate model spatial covariance biases cause the largest reductions in correlation coefficients and sharply reduce skill outside of the extratropical Northern Hemisphere. This effect occurs for both sets of biased-model reconstructions, but is more pronounced when using a CESM prior to reconstruct an MPI target. Results for the other skill metrics show similar behavior (Figures S1, S2, and S3).

We next compare the results for the most realistic DA experiments (the noisy-proxy, temporal-attrition, biased-model cases) to the corresponding PPR pseudo-proxy reconstructions. Given the strict reconstruction radius in PPR, and the spatial pattern of DA skill, we consider only the extratropical Northern Hemisphere in our discussion. The skill metrics for the mean extratropical time series are similar for the two methods (Table S2). The regional spatial correlations of the DA and PPR reconstructions (Figures 3, S4) are also comparable: each exhibits correlations with the target field greater than 0.7 in Scandinavia, central Asia, and western Canada, and these regions correspond to the best coverage by the proxy network. Similarly, both methods exhibit low correlations in southeastern Canada and northeastern Eurasia. Notably, the DA exhibits a broader spatial region of high correlation than PPR, and DA correlations are higher than PPR values at nearly all grid points. We observe similar patterns for RMSE values, which are lower in the DA reconstructions at most grid points. Standard deviation ratios indicate that the DA reconstructions underestimate temporal temperature variability, but this effect is less severe near the proxy sites. In contrast with DA, PPR time series σ ratios neither strictly overestimate nor strictly underestimate temporal variability, instead demonstrating a mixed response over the hemisphere. In general, the DA reconstructions underestimate variability more than PPR. Mean biases are comparable, with both methods exhibiting similar spatial patterns and bias magnitudes, although it is interesting to note that the spatial patterns of bias change markedly with the target field (Figure S4).

b. Real assimilation

Validation statistics for the mean extratropical MJJA time series are similar across all priors (Table 2) with mean correlations of 0.70, RMSE of 0.19 °C, and absolute mean bias of 0.06 °C. Temporal variability is close to the target value with mean standard deviation ratios of 1.11. The reconstructed time series obtained using different model priors (Figure S5) are most similar when all proxy records are available, with a mean range of 0.22 °C over the period of full coverage (1750-1988 CE; $n = 54$). However, the reconstructed time series diverge as the network become more sparse, with a range of 0.30 °C in 1000 CE ($n = 23$) and 0.76 °C in the first year of the reconstruction (750 CE; $n = 4$). The ensemble mean time series exhibits similar skill values as the reconstructions for the individual models with a correlation of 0.72, RMSE of 0.18 °C, temporal σ ratio of 1.06, and a mean bias of 0.05 °C.

Figure 4 illustrates the mean extratropical MJJA time series for the DA ensemble-mean reconstruction. Here, we quantify the uncertainty of the DA time series using two methods. Our first measure of uncertainty is derived from the DA posterior ensembles, as detailed in Section 2b. We also determine the uncertainty that arises from the selection of different model priors in the DA method. This is an important structural uncertainty, but this metric underestimates the total uncertainty in the reconstructed temperature time series. We compare our ensemble-mean time series to the analogous time series extracted from the Berkeley Earth instrumental record and the Anchukaitis et al. (2017) NTREND PPR reconstruction. The series shows similar behavior as the Berkeley Earth instrumental series from 1880-1988 CE, although both the DA and PPR reconstructions of Anchukaitis et al. (2017) diverge from this dataset over the period from 1850-1879 CE, which may reflect a warm bias in the early instrumental temperature record (Parker 1994; Frank et al. 2007; Böhm et al. 2010) and the limited spatial coverage of earliest instrumental period (Rohde et al. 2013; Anchukaitis et al. 2017). The DA and PPR time series show similar behavior over most of the record, with a correlation coefficient of 0.88. The temporal variability of the PPR time series is generally higher than that of DA time series; however, prior to about 1400 CE, the difference between the series' running standard deviations begins to increase with substantial divergence prior to about 1100 CE. This effect is driven by a decrease in the variability of the DA time series and reflects the reduction in update magnitudes in the assimilation as the proxy network shrinks.

Spatial validation statistics in the real assimilation show similar patterns to those observed in the pseudo-proxy experiments (Figure 5). Correlation coefficients and standard deviation ratios are highest over Scandinavia, central Asia, and northwestern North America, the regions of densest network coverage. Correlation coefficients approach 0.8 near proxy sites, and standard deviation ratios approach that of target values. RMSE values are typically less than 0.6 °C, but rise to values near 1 °C over the North Pacific, central Canada, and southern Siberia. Mean biases display maxima over central Canada and northeastern Asia, minima over Greenland and southern Siberia, and magnitudes typically below 0.5 °C. Away from the proxy sites, temporal variability is underestimated, particularly over the oceans. However, most land grid points exhibit σ ratios near 1 with a slight overestimate in central Asia and northern Japan. Much of the temporal variability in the extratropical mean time series is driven by land grid points, and this tendency helps reconcile Figure 5 with extratropical mean time series σ ratios near 1.

Independent proxy validation statistics (Table 4) show median correlation coefficients near 0.5, and RMSE values near 1°C. Temporal variability is underestimated relative to the target series with σ ratios typically between 0.3 and 0.4. Mean biases are variable and depend on the prior model used. Given the sparsity of the NTREND network, removing even a single proxy record from the assimilation can substantially reduce the ability to reconstruct temperature anomalies at nearby grid cells. Consequently, the leave-one-out assimilation process we use to assess independent proxy skill almost certainly underestimates overall field validation skill. Nevertheless, these values are comparable to previous efforts with median correlation coefficients somewhat higher than those in Hakim et al. (2016) and Tardif et al. (2019).

c. Epochal temperature changes

We next examine the temperature change between the Medieval Climate Anomaly (MCA; 950 - 1250 CE) and the Little Ice Age (LIA; 1450 - 1850 CE) within our reconstruction framework (Masson-Delmotte et al. 2013; Anchukaitis et al. 2017). Figure 6 shows these anomaly patterns reconstructed using different model priors. The maps indicate warmer temperatures during the MCA at nearly all high-latitude grid cells with the largest MCA-LIA temperature change typically over northeastern Canada. However, the magnitude of this anomaly varies across the reconstructions with values ranging from over 1.6 °C (CCSM4, MIROC, MPI) to less than 0.8 °C (IPSL, FGOALS). Aside from a warm anomaly in northeastern Canada, the spatial pattern also varies by model prior. Many reconstructions show stronger anomalies near Fennoscandia, northeastern Asia, and northwestern North America, but these patterns do not occur in all models. Furthermore, these patterns vary in location, relative strength, and absolute magnitude for different models priors. For example, in the MIROC reconstruction, the maximum warm anomaly in northeastern Asia occurs near 60 °N with a magnitude near 1.2 °C. This feature is stronger than the western Asian feature, which occurs north of the Caspian Sea and has a maximum magnitude near 0.8 °C. By contrast, the anomaly map for CESM places northeastern Asian warming closer to 72 °N. Its maximum is near 0.8 °C and is comparable to the maximum of the western Asia feature, which is focused on Fennoscandia. Finally, the northeastern Asia feature does not occur in the CCSM4 reconstruction, and the western Asia feature extends broadly from Scandinavia to east of the Caspian Sea. Overall, the HadCM3 reconstruction is perhaps the most atypical: aspects of the previously mentioned features are present in its anomaly map, but it exhibits larger anomalies over most of the hemisphere and is more spatially variable than the other reconstructions.

Comparing the MCA-LIA difference for our ensemble-mean reconstruction with other CFRs (Figure 7) further emphasizes the sensitivity of this pattern to reconstruction methods. Our anomaly map is unsurprisingly most similar to that of Anchukaitis et al. (2017). Both show the largest temperature change over Fennoscandia and northeastern Canada. The magnitudes of these anomalies are comparable with the exception of northeastern Canada. In the Anchukaitis et al. (2017) reconstruction, this region exhibits anomalously high medieval temperatures (> 3 °C), which they attribute to an apparent detrending artifact in the QUEw record. By contrast, our DA reconstruction produces a maximum medieval anomaly of 1 °C for this region, in better agreement with other proxy reconstructions (e.g. 0-1.5°C; Sundqvist et al. 2014). Comparing the results of this study to the LMR 2.1 (Tardif et al. 2019) and Neukom et al. (2019), we observe that both NTREND DA and Neukom et al. (2019) exhibit a positive anomaly over most of the high-latitude Northern Hemisphere; however, the anomalies in the Neukom et al. (2019) product have much larger magnitudes and the maxima of the North America features occur in different locations. The LMR2.1 product exhibits an anomaly pattern notably different from the other reconstructions, with a strong positive anomaly in the Arctic Ocean north of Siberia. Since the Guillet et al. (2017) reconstruction reflects highpass filtered reconstructed temperatures, we do not consider it in this comparison.

d. Volcanic Response

We next examine the composite mean response to major tropical volcanic eruptions. We use eruption years ($n = 20$) with a global forcing magnitude equal to or larger than the 1884 Krakatoa eruption: this set consists of 916, 1108, 1171, 1191, 1230, 1258, 1276, 1286, 1345, 1453, 1458, 1595, 1601, 1641, 1695, 1809, 1815, 1832, 1836, and 1884 CE (Sigl et al. 2015; Anchukaitis et al. 2017). In the composite mean maps, we calculate event anomalies by removing the mean reconstructed MJJA field from the five years prior to each volcanic event. We only consider grid points with reconstructed values for at least 6 eruptions. The NTREND DA reconstructions using different model priors show broadly similar responses to large tropical volcanic eruptions (Figure 8). The spatial pattern is characterized by a strong cold anomaly in northern Canada and a second region of cooling extending from Fennoscandia to central Asia. However, the extent and magnitude of these vary between the different reconstructions. For example, the northern Asia cooling anomaly in the CCSM4 reconstruction covers an area about 1.5 times as wide zonally as the same feature in the CESM reconstruction. Similarly, the northern Canada cooling anomaly for the MRI reconstruction includes most of the Hudson Bay, whereas the CSIRO reconstruction's anomaly does not even reach the Hudson Bay's western edge. The magnitudes of cooling anomalies are similarly variable. The maximum magnitude of the northern Canada anomaly ranges from about 0.6 °C (CSIRO) to 1.5 °C (CCSM4, CESM), and a similar range occurs for the western Asia feature. Several regions also exhibit markedly spatial patterns across the 10 reconstructions. In particular, the response in central North America and eastern Asia appears highly sensitive to the choice of model prior.

Comparing the volcanic pattern for the ensemble-mean with the other CFRs (Figure 9) shows larger differences in spatial patterns, magnitudes, and even sign of the anomalies. In general, most CFRs show some combination of cooling anomalies in northern North America and northern Asia, with a slight warming anomaly in the North Pacific. However, these features are not present in all the CFRs and vary in maximum magnitude. The NTREND DA ensemble-mean, Anchukaitis et al. (2017), and Guillet et al. (2017) products all exhibit the northern Canada and western Asia cooling features and the spatial extent is similar for the two NTREND products. In contrast, the Guillet et al. (2017) Canadian feature is centered farther east, and its northern Asian feature is stronger (near 1.5 °C) with a maximum more strongly localized to northern Siberia. These two features are also present in Zhu et al. (2020), but maximum cooling is smaller in magnitude and near 0.6 °C. The LMR2.1 does not show a distinct northern Asia terrestrial cooling, although a composite anomaly of 0.6 C is reconstructed in the Arctic Ocean north of Siberia. This reconstruction also demonstrates a North American response pattern similar to Zhu et al. (2020) with a reduced magnitude of cooling in northern Canada. The Neukom et al. (2019) product again shows the largest anomalies, with values greater than 1.5 °C over much of northern Siberia and Fennoscandia. This feature does not extend as far south as in the NTREND DA ensemble-mean but is zonally wider. Neukom et al. (2019) also show a single strong North American feature with cooling magnitudes near 1.2 °C. Interestingly, Neukom et al. (2019) exhibits a North Pacific warming response that strengthens one year after the volcanic event, a feature also evident in the Anchukaitis et al. (2017) reconstruction that may reflect changes in atmospheric circulation following an eruption (e.g. Robock 2000; Stenchikov et al. 2006; Christiansen 2008; Schneider et al. 2009)

4. Discussion

The pseudo-proxy experiments indicate that high reconstruction skill for the assimilated NTREND network is limited to the extratropical Northern Hemisphere when using biased climate model priors. This finding supports work by Franke et al. (2020) and suggests that analyses of temperatures using the NTREND network should be limited to this region, consistent with Wilson et al. (2016) and Anchukaitis et al. (2017). In comparison with PPR, our DA method exhibits similar skill at reconstructing mean extratropical MJJA time series using the NTREND network, but also provides continuous field estimates of past temperature and improves the spatial correlation and RMSE. We suggest this improvement arises at least in part from the contrast between PPR's strict-limited search radius and the DA's longer localization radii. Many NTREND sites exhibit statistically significant covariance with the MJJA temperature field outside of PPR's 2000 km maximum search radius (see Figure 5 of Anchukaitis et al. (2017)), and these distal covariances are not used to improve the PPR reconstruction. By contrast, the DA uses no localization in these pseudo-proxy experiments and if the model prior provides a good estimate of a proxy site's field covariance, the proxy record can inform the reconstruction of distal grid points. Ultimately, these results suggest that our DA method does improve on the spatial component of NTREND (Anchukaitis et al. 2017) for reconstructing a Northern Hemisphere climate history of the Common Era from the NTREND network.

The consistency with which the DA underestimates the temporal variability of the target field, particularly over the oceans and distal to the actual proxy sites, requires consideration. In this study, we focus on time series derived from the ensemble-mean of the posterior at each time step. Because of this focus on the ensemble-mean, however, at times we neglect the width of the full posterior ensemble. Like many offline EnSRF studies (e.g. Hakim et al. 2016; Dee et al. 2016; Steiger et al. 2018), our method uses the same prior ensemble in each time step; thus, the ensemble-mean of the prior is constant through time. As the proxy network becomes more sparse in space and time, the magnitudes of updates decrease, and the posterior ensemble will then more closely resemble the prior. When this occurs, a reconstructed ensemble-mean time series will more closely resemble the constant prior, and the temporal variability of this time series will approach zero. However, this reduction in variability for the posterior ensemble-mean is balanced by the width of the full posterior, which will remain near the spread of the prior ensemble. Incorporating the width of the posterior with ensemble-mean time series can produce a range that encompasses target time-series variability, but using these ranges for climate analysis or validation metrics can be difficult. Hence, we emphasize that users of DA products with constant priors should carefully consider how changes in the proxy network affect the temporal variability of reconstructed ensemble-mean time series. For example, in this study, a decrease in the number of proxy records causes the temporal variability of the reconstructed extratropical mean MJJA time series to decrease prior to about 1100 CE (Figure 4). Also, grid point time series far from the proxy sites have lower σ ratios (Figure 5), so regions far from the proxy network will exhibit temperature anomalies with smaller magnitudes. Finally, we note that allowing the model prior to vary in each time step can help mitigate these effects, which argues for the future use when possible of evolving offline priors or online assimilation techniques (e.g. Perkins and Hakim 2017).

The results of this study also highlight the sensitivity of the DA reconstructions to the model prior. In the pseudo-proxy experiments, the perfect-model reconstructions suggest high skill over broad spatial scales; for example, even with the spatially limited NTREND network, the CESM perfect-model experiments show correlations greater than 0.6 with the target field in regions south of the equator. However, the introduction of model bias (effectively, a mismatch between the 'true' spatial covariance and that of prior) isolates high skill to regions near the proxy sites. Correlation between the pseudo-proxy reconstruction and the know target field outside of these regions is drastically reduced in magnitude. Compared to this factor, network attrition and noisy proxies cause relatively less reductions to DA skill, a finding in agreement with Dee et al. (2016). Given this potential for perfect-model experiments to exaggerate the magnitude and spatial extent of DA skill, we encourage future DA proof-of-concept and sensitivity studies to consider perfect-model experiments in conjunction with biased-model cases.

Reconstructions are most sensitive to the prior when the proxy network is sparse in space and time. For example, despite using the same proxy network and reconstruction technique, mean extratropical MJJA time series diverge by more than 0.5 °C in the earliest parts of the reconstruction when the network is limited (Figure S5). The use of different priors also produces noticeable differences in spatial MCA-LIA temperature anomaly patterns (Figure 6), largely because of the small size of the proxy network during the MCA. In contrast, the volcanic response maps present a more consistent spatial pattern (Figure 8), which we attribute to the larger size of the proxy network during most of the large volcanic events and perhaps the magnitude of the forced response. However, the volcanic response maps still exhibit different spatial patterns in regions like east Asia where the proxy network is sparse.

The prior sensitivity and temporal variability effects underscore the importance of understanding how the proxy network affects the quality of the reconstruction (Esper et al. 2005; Wang et al. 2014). A key feature of DA techniques is the ability to estimate reconstruction uncertainty in each time step from the width of the posterior ensemble. Figure 10 provides an example of such an analysis for the DA ensemble-mean by examining the temperature response following the 1257 CE (Lavigne et al. 2013) and 1600 CE (De Silva and Zielinski 1998) volcanic eruptions in conjunction with the full posterior width. The uncertainty maps for both events show maxima in central North American and northeastern Asia and suggest that associated temperature anomalies should be interpreted more cautiously. Notably, these regions correspond to areas that are also sensitive to the prior in Figure 8. By contrast, central Asia, Fennoscandia, central Europe, and southwestern Canada exhibit a narrow posterior for both events, so volcanic anomalies in these regions are better constrained. Interestingly, the temperature response in 1601 CE is relatively small over much of central Europe and reconstruction uncertainty is relatively low, which suggests this feature may be a robust feature of the post-eruption climate anomaly. In addition to supporting analysis of reconstructed climate features, these uncertainty estimates can help identify regions that would benefit from increased network density, as in Comboul et al. (2015). In particular, we observe that northern North America and eastern Siberia would benefit from the development of new millennial-length temperature-sensitive tree-ring records.

The CFR comparison reveals the highly variable nature of spatial patterns and magnitudes of reconstructed temperature anomalies that result from different selections of proxy networks, target fields, and reconstruction methodologies. For example, despite using the same proxy network and target field, the NTREND DA ensemble-mean and PPR result from Anchukaitis et al. (2017) have MCA-LIA anomalies that differ by over 2 °C in northeastern Canada (Figure 7), which relates to the outsize effect of the local QUEw record on the Anchukaitis et al. (2017) reconstruction. We note that the localization radii used in our reconstructions (≥ 9500 km) allow proxies to influence grid cells farther away than the strict 2000 km search radius used by Anchukaitis et al. (2017), so distant proxies are able to counter the effects of the anomalous QUEw record in the DA. Within a DA framework, reconstructed climate responses are highly variable, particularly for MCA-LIA anomalies. These differences result from targeting different fields and leveraging different proxy networks. Aside from spatial and temporal coverage, we note that using proxy records that are not strictly temperature sensitive can introduce structural biases relative to other temperature CFRs. For example, the LMR2.1 reconstruction includes proxies that are not only sensitive to temperature, which could possibly reduce update magnitudes and help explain the smaller magnitudes of the volcanic responses. Similarly, the Neukom et al. (2019) DA product and LMR2.1 incorporate proxies like corals and lake-sediments that are not present in the tree-ring based CFRs, and it is possible that these records influence the large magnitudes of the Neukom et al. (2019) DA climate responses or the atypical LMR2.1 MCA-LIA spatial pattern. However, we emphasize that these hypotheses are strictly speculative at this moment and that the differences in reconstructed climate response by themselves do not indicate whether one proxy network or reconstruction is superior to another in representing past climate variability. Instead, our CFR comparison highlights that, despite the recent decades of progress in understanding both methods and paleoclimate data (Hughes and Ammann 2009; Frank et al. 2010; Smerdon et al. 2011; Tingley et al. 2012; Wang et al. 2014; Smerdon and Pollack 2016; Christiansen and Ljungqvist 2017; Esper et al. 2018), differences in reconstructions of past temperature still arise when using different proxy networks, different target seasons, and making different reconstruction choices, and these differences fundamentally influence our interpretation of the temperature response to radiative forcing (c.f. Wang et al. 2015). This observation calls for a revival of paleo-reconstruction intercomparison projects (e.g. Ammann 2008; Graham and Wahl 2011) in order to examine the behavior, strengths, and weaknesses of different proxy networks and reconstruction choices in a systematic and community-driven manner. Furthermore, such an effort would help identify regions with consistently large reconstruction uncertainties and indicate where to prioritize the development of new records.

5. Conclusions

In this study, we assimilate a small, temperature-sensitive tree-ring network based on expert assessment (Frank et al. 2010) to reconstruct summer (MJJA) temperature anomalies from 750-1988 CE. Our method is skillful in the extratropical Northern Hemisphere and improves on the spatial reconstruction of Anchukaitis et al. (2017), thereby providing a new dataset with which to examine temperature dynamics and climate response to radiative forcing over the last millennium. In a set of pseudo-proxy experiments, we find that our method is sensitive to climate model biases, so we perform an ensemble of reconstructions using 10 different climate model priors. Reconstructed temperature anomalies are sensitive to the selection of the model prior when the proxy network becomes sparse in space and time, but reconstructed spatial patterns and time series converge to more consistent values as the proxy network grows. As a consequence of using static offline priors, our method underestimates temporal variability when the proxy network becomes small, which argues for the future use of evolving offline priors or online assimilation techniques in DA paleoclimate reconstructions. The influence of the proxy network coverage on the reconstructions emphasizes the importance of analyzing reconstructed temperature anomalies in conjunction with estimates of their uncertainty. These uncertainty estimates emerge naturally for both spatial fields and time series from the DA posterior ensembles and are an enhancement over previous reconstructions using the NTREND dataset. In addition to gauging reconstruction validity, the uncertainty estimates identify regions that would benefit from additional proxy records and support the development of more millennial-length temperature-sensitive tree-ring records in treeline North America and eastern Siberia especially. Comparison of our reconstruction with other temperature CFRs indicates that reconstructed temperature anomalies have highly variable spatial patterns and magnitudes, even within similar reconstruction frameworks and proxy network. These different climate responses call for a renewed paleo-reconstruction intercomparison framework in which to systematically examine the effects of network selection across reconstruction techniques and prioritize regions for future record development (Anchukaitis and McKay 2015).

Data availability statement. The NTREND proxy data and the earlier reconstructions are available from the NOAA NCEI World Data Service for Paleoclimatology (`https://www.ncdc.noaa.gov/paleo-search/study/19743`). The NTREND-DA ensemble reconstructions will be available from NOAA NCEI World Data Service for Paleoclimatology ([insert url here once accepted]). Model priors from the CMIP5 and CESM LME are available on the Earth System Grid (`https://esgf-node.llnl.gov/projects/esgf-llnl/`) and the NCAR Climate Data Gateway (`https://www.earthsystemgrid.org/`), respectively. The data and code used to run these analyses and a function reproducing the results and figures from this paper are available at `https://doi.org/10.5281/zenodo.3989941`.

Acknowledgments. The authors acknowledge support from the Climate Program Office of the National Oceanographic and Atmospheric Administration (NOAA grants NA18OAR4310420 to KJA, NA18OAR4310426 to JEG and FZ, and NA18OAR4310422 to GJH). GJH also acknowledges support from the NSF through grant AGS–1702423. JMK was partially supported by NSF grant AGS-1803946. JET and JMK acknowledge support from NSF grant #AGS-1602301 and Heising-Simons Foundation grant #2016-05. We acknowledge the World Climate Research Programme's Working Group on Coupled Modelling, which is responsible for CMIP, and we thank the climate modeling groups (listed in Table 1 of this paper) for producing and making available their model output.

APPENDIX

Data Assimilation Methods

A1. The Ensemble Kalman Filter

Our data assimilation method uses an ensemble Kalman filter approach (Evensen 1994; Steiger et al. 2014; Hakim et al. 2016) to solve the update equation:

$$\mathbf{X_a} = \mathbf{X_p} + \mathbf{K}(\mathbf{Y} - \mathbf{Y_e}) \tag{A1}$$

in each reconstructed annual time step. Here $\mathbf{X_p}$ is an initial ensemble of plausible climate states, an n x m matrix where n is the number of state variables and m is the number of ensemble members. $\mathbf{X_a}$ is the updated ensemble (the analysis), also an n x m matrix. $\mathbf{Y}$ is a d x m matrix of observed proxy values, where d is the number of available proxy records in a given time step. We do not perturb observed proxy values for different ensemble members (see Whitaker and Hamill 2002), so $\mathbf{Y}$ is a matrix with constant rows. $\mathbf{Y_e}$ is a d x m matrix consisting of model estimates of the proxy values. Each element $\mathrm{y}_{\mathrm{e}_{jk}}$ is determined by applying the PSM for the j^{th} proxy site to the k^{th} climate state in the ensemble via Equation 1. Note in Equation 1 that $\mathbf{y}_{\mathbf{e}_j}$ is the j^{th} row of $\mathbf{Y_e}$ and $\mathbf{T}_j$ is 1 x m. $\mathbf{K}$ is the Kalman Gain, an n by d matrix that weights the covariance of proxy sites with the target field by the uncertainties in the proxy observations and estimates.

We use an EnKF variant known as the ensemble square root Kalman filter (EnSRF; Andrews 1968), which removes the need for perturbed observations (Whitaker and Hamill 2002). In the EnSRF formulation, ensemble deviations are updated separately from the mean, as per:

$$\bar{\mathbf{x}}_\mathbf{a} = \bar{\mathbf{x}}_\mathbf{p} + \mathbf{K}(\bar{\mathbf{y}} - \bar{\mathbf{y}}_\mathbf{e}) \tag{A2}$$

$$\mathbf{X}'_{\mathbf{a}} = \mathbf{X}'_{\mathbf{p}} - \tilde{\mathbf{K}}\mathbf{Y}'_{\mathbf{e}} \tag{A3}$$

where an overbar ($\bar{\mathbf{x}}$) denotes an ensemble average, and a tick ($\mathbf{X}'$) indicates deviations from an ensemble mean. Here, the ensemble mean is updated via the standard Kalman gain ($\mathbf{K}$):

$$\mathbf{K} = \mathbf{PH}^{\mathrm{T}}[\mathbf{HPH}^{\mathrm{T}} + \mathbf{R}]^{-1} = \mathrm{cov}(\mathbf{X_p}, \mathbf{Y_e}) \times [\mathrm{cov}(\mathbf{Y_e}, \mathbf{Y_e}) + \mathbf{R}]^{-1} \tag{A4}$$

and the deviations are updated via an adjusted gain ($\tilde{\mathbf{K}}$):

$$\begin{aligned} \tilde{\mathbf{K}} &= \mathbf{PH}^{\mathrm{T}}[(\sqrt{\mathbf{HPH}^{\mathrm{T}} + \mathbf{R}})^{-1}]^{\mathrm{T}}[\sqrt{\mathbf{HPH}^{\mathrm{T}} + \mathbf{R}} + \sqrt{\mathbf{R}}]^{-1} \\ &= \mathrm{cov}(\mathbf{X_p}, \mathbf{Y_e}) \times [(\sqrt{\mathrm{cov}(\mathbf{Y_e}, \mathbf{Y_e}) + \mathbf{R}})^{-1}]^{\mathrm{T}}[\sqrt{\mathrm{cov}(\mathbf{Y_e}, \mathbf{Y_e}) + \mathbf{R}} + \sqrt{\mathbf{R}}]^{-1} \end{aligned} \tag{A5}$$

Here, $\mathbf{P}$ is the model covariance (n x n), and $\mathbf{R}$ denotes the observation error-covariance matrix (d x d). Nominally, $\mathbf{H}$ is a d x n observation matrix used to determine proxy-state variable and proxy-proxy covariance matrices from $\mathbf{P}$. However, in practice we determine these covariance matrices using the proxy value estimates ($\mathbf{Y_e}$) and prior ensemble ($\mathbf{X_p}$). We do not consider correlated measurement errors in this study, so $\mathbf{R}$ is a diagonal matrix whose elements are the observation uncertainties determined from the variances of the residuals for the PSM regressions. This formulation is therefore mathematically equivalent to the serial update schemes used in other studies (e.g. Steiger et al. 2014) when using linear PSMs and no covariance localization.

A2. Covariance Localization

We implement a covariance localization scheme, modifying the Kalman Gain equations to:

$$\begin{aligned} \mathbf{K} &= \mathbf{W}_{\mathrm{loc}} \circ \mathbf{PH}^{\mathbf{T}}[\mathbf{Y}_{\mathrm{loc}} \circ \mathbf{HPH}^{\mathbf{T}} + \mathbf{R}]^{\mathbf{-1}} \\ &= \mathbf{W}_{\mathrm{loc}} \circ \mathrm{cov}(\mathbf{X_p}, \mathbf{Y_e}) \times [\mathbf{Y}_{\mathrm{loc}} \circ \mathrm{cov}(\mathbf{Y_e}, \mathbf{Y_e}) + \mathbf{R}]^{\mathbf{-1}} \end{aligned} \tag{A6}$$

and

$$\begin{aligned}\tilde{\mathbf{K}} &= \mathbf{W}_{\text{loc}} \circ \mathbf{PH}^{\mathbf{T}} [(\sqrt{\mathbf{Y}_{\text{loc}} \circ \mathbf{HPH}^{\mathbf{T}} + \mathbf{R}})^{-\mathbf{1}}]^{\mathbf{T}} [\sqrt{\mathbf{Y}_{\text{loc}} \circ \mathbf{HPH}^{\mathbf{T}} + \mathbf{R}} + \sqrt{\mathbf{R}}]^{-\mathbf{1}} \\ &= \mathbf{W}_{\text{loc}} \circ \text{cov}(\mathbf{X_p}, \mathbf{Y_e}) \times [(\sqrt{\mathbf{Y}_{\text{loc}} \circ \text{cov}(\mathbf{Y_e}, \mathbf{Y_e}) + \mathbf{R}})^{-\mathbf{1}}]^{\mathbf{T}} [\sqrt{\mathbf{Y}_{\text{loc}} \circ \text{cov}(\mathbf{Y_e}, \mathbf{Y_e}) + \mathbf{R}} + \sqrt{\mathbf{R}}]^{-\mathbf{1}}.\end{aligned} \tag{A7}$$

Here, $\mathbf{W}_{\text{loc}}$ (n x d) and $\mathbf{Y}_{\text{loc}}$ (d x d) are matrices of covariance localization weights applied to the covariance of proxy sites with model grid cells ($\mathbf{W}_{\text{loc}}$) and proxy sites with one another ($\mathbf{Y}_{\text{loc}}$). We implement localization weights as a fifth order Gaspari-Cohn polynomial (Gaspari and Cohn 1999) applied to the distance between proxy sites and model grid cells ($\mathbf{W}_{\text{loc}}$), or proxy sites with one another ($\mathbf{Y}_{\text{loc}}$). The weights are applied to the relevant covariance matrices via element-wise multiplication and the resulting reduced covariance matrices are then used in the Kalman filter.

The localization radius is an important free parameter in this method. As mentioned, localization can help reduce the effects of climate model covariance biases and thus must be assessed independently for different model priors, reconstruction targets, and proxy networks. Here, we select localization radii using a two step process. In the first step, for a given model prior and target field, we assimilate the proxy network from 1901-1988 CE using each localization radius from 250 km to 50,000 km in steps of 250 km. We also perform an run with an infinite radius (i.e. no localization). We then extract the reconstructed mean extratropical MJJA temperature time series from each of these DA reconstructions.

To limit the sensitivity of this method to stochastic effects arising from the selection of the calibration period (Christiansen et al. 2009), we next perform multiple split-sample calibration-validations on the set of 201 time series. Here we use each set of 44 contiguous years from 1901-1988 CE once as a calibration interval and once as a validation interval for a total of 88 total calibration-validation procedures per time series. For each calibration-validation procedure we determine which time series has the σ ratio closest to 1 in the calibration interval. We assess skill metrics for this time series over the validation interval and record the associated localization radius as optimal for that particular calibration interval. We repeat this procedure for each calibration interval and use the median optimal radius as the final localization radius in the full assimilation. We also report the median of the skill metrics assessed over the 88 validation intervals as the skill of the mean extratropical MJJA time series in the full assimilation.

In our method, we select localization radii using a σ ratio selection criterion. However, in the development of this method, we also tested an RMSE selection criterion. We find that correlation coefficients, RMSE values, and mean biases of the reconstructed mean extratropical MJJA time series are all insensitive to the choice of selection criteria (Table 2, Table A1), but that σ ratios are more sensitive. Specifically, mean σ ratios are near 0.8 for the RMSE selection criterion, but rise to 1.11 for the σ ratio scheme. Since the σ ratio localization selection criteria brings the σ ratio skill metric closer to 1 without appreciably altering the other skill metrics and because of the tendency for our DA method to underestimate temporal variability, we use σ ratios as the selection criteria for the localization radii for the full assimilation.

References

Acevedo, W., B. Fallah, S. Reich, and U. Cubasch, 2017: Assimilation of pseudo-tree-ring-width observations into an atmospheric general circulation model. *Climate of the Past*, **13 (5)**, 545–557.

Ammann, C., 2008: The paleoclimate reconstruction challenge. *PAGES News*, **16 (1)**, 4.

Anchukaitis, K. J., and N. McKay, 2015: PAGES2k: Advances in climate field reconstructions. *PAGES Magazine*, **22 (2)**, 98.

Anchukaitis, K. J., and Coauthors, 2017: Last millennium Northern Hemisphere summer temperatures from tree rings: Part II, spatially resolved reconstructions. *Quaternary Science Reviews*, **163**, 1–22.

Andrews, A., 1968: A square root formulation of the Kalman covariance equations. *AIAA Journal*, **6 (6)**, 1165–1166.

Annan, J., and J. Hargreaves, 2012: Identification of climatic state with limited proxy data. *Climate of the Past*, **8 (4)**, 1141–1151.

Bhend, J., J. Franke, D. Folini, M. Wild, and S. Brönnimann, 2012: An ensemble-based approach to climate reconstructions. *Climate of the Past*, **8 (3)**, 963–976.

Björklund, J., B. E. Gunnarson, K. Seftigen, J. Esper, and Coauthors, 2014: Blue intensity and density from northern fennoscandian tree rings, exploring the potential to improve summer temperature reconstructions with earlywood information. *Climate of the Past*, **10 (2)**, 877–885.

Böhm, R., P. D. Jones, J. Hiebl, D. Frank, M. Brunetti, and M. Maugeri, 2010: The early instrumental warm-bias: a solution for long central european temperature series 1760–2007. *Climatic Change*, **101 (1-2)**, 41–67.

Braconnot, P., S. P. Harrison, M. Kageyama, P. J. Bartlein, V. Masson-Delmotte, A. Abe-Ouchi, B. Otto-Bliesner, and Y. Zhao, 2012: Evaluation of climate models using palaeoclimatic data. *Nature Climate Change*, **2 (6)**, 417–424.

Chen, Z., and Coauthors, 2003: Bayesian filtering: From Kalman filters to particle filters, and beyond. *Statistics*, **182 (1)**, 1–69.

Christiansen, B., 2008: Volcanic eruptions, large-scale modes in the northern hemisphere, and the el niño–southern oscillation. *Journal of Climate*, **21 (5)**, 910–922.

Christiansen, B., and F. C. Ljungqvist, 2017: Challenges and perspectives for large-scale temperature reconstructions of the past two millennia. *Reviews of Geophysics*, **55 (1)**, 40–96.

Christiansen, B., T. Schmith, and P. Thejll, 2009: A surrogate ensemble study of climate reconstruction methods: Stochasticity and robustness. *Journal of Climate*, **22 (4)**, 951–976.

Comboul, M., J. Emile-Geay, G. J. Hakim, and M. N. Evans, 2015: Paleoclimate sampling as a sensor placement problem. *Journal of Climate*, **28**, 7717–7740, doi:10.1175/JCLI-D-14-00802.1.

Cook, E. R., K. J. Anchukaitis, B. M. Buckley, R. D. D'Arrigo, G. C. Jacoby, and W. E. Wright, 2010a: Asian monsoon failure and megadrought during the last millennium. *Science*, **328 (5977)**, 486–489.

Cook, E. R., K. R. Briffa, and P. D. Jones, 1994: Spatial regression methods in dendroclimatology: a review and comparison of two techniques. *International Journal of Climatology*, **14 (4)**, 379–402.

Cook, E. R., P. J. Krusic, K. J. Anchukaitis, B. M. Buckley, T. Nakatsuka, M. Sano, and Coauthors, 2013: Tree-ring reconstructed summer temperature anomalies for temperate East Asia since 800 CE. *Climate Dynamics*, **41 (11-12)**, 2957–2972.

Cook, E. R., D. M. Meko, D. W. Stahle, and M. K. Cleaveland, 1999: Drought reconstructions for the continental United States. *Journal of Climate*, **12 (4)**, 1145–1162.

Cook, E. R., R. Seager, R. R. Heim Jr, R. S. Vose, C. Herweijer, and C. Woodhouse, 2010b: Megadroughts in North America: Placing IPCC projections of hydroclimatic change in a long-term palaeoclimate context. *Journal of Quaternary Science*, **25 (1)**, 48–61.

Cowtan, K., and R. G. Way, 2014: Coverage bias in the HadCRUT4 temperature series and its impact on recent temperature trends. *Quarterly Journal of the Royal Meteorological Society*, **140 (683)**, 1935–1944.

De Silva, S. L., and G. A. Zielinski, 1998: Global influence of the AD 1600 eruption of Huaynaputina, Peru. *Nature*, **393 (6684)**, 455–458.

Dee, S., J. Emile-Geay, M. Evans, A. Allam, E. Steig, and D. Thompson, 2015: PRYSM: An open-source framework for PRoxY System Modeling, with applications to oxygen-isotope systems. *Journal of Advances in Modeling Earth Systems*, **7 (3)**, 1220–1247.

Dee, S. G., N. J. Steiger, J. Emile-Geay, and G. J. Hakim, 2016: On the utility of proxy system models for estimating climate states over the Common Era. *Journal of Advances in Modeling Earth Systems*, **8 (3)**, 1164–1179.

Delworth, T. L., and M. E. Mann, 2000: Observed and simulated multidecadal variability in the Northern Hemisphere. *Climate Dynamics*, **16 (9)**, 661–676.

Deser, C., A. Phillips, V. Bourdette, and H. Teng, 2010: Uncertainty in climate change projections: the role of internal variability. *Climate Dynamics*, **38 (3-4)**, 527–546, doi: 10.1007/s00382-010-0977-x.

Dubinkina, S., and H. Goosse, 2013: An assessment of particle filtering methods and nudging for climate state reconstructions. *Climate of the Past*, **9 (3)**, 1141–1152.

Esper, J., D. C. Frank, R. J. Wilson, and K. R. Briffa, 2005: Effect of scaling and regression on reconstructed temperature amplitude for the past millennium. *Geophysical Research Letters*, **32 (7)**.

Esper, J., and Coauthors, 2018: Large-scale, millennial-length temperature reconstructions from tree-rings. *Dendrochronologia*, **50**, 81–90, doi:10.1016/j.dendro.2018.06.001.

Evans, M., A. Kaplan, M. Cane, and R. Villalba, 2001: Globality and optimality in climate field reconstructions from proxy data. *Interhemispheric Climate Linkages*, Elsevier, 53–XV.

Evans, M. N., A. Kaplan, and M. A. Cane, 2002: Pacific sea surface temperature field reconstruction from coral δ^{18}O data using reduced space objective analysis. *Paleoceanography*, **17 (1)**, doi:10.1029/2000PA000590.

Evans, M. N., S. E. Tolwinski-Ward, D. M. Thompson, and K. J. Anchukaitis, 2013: Applications of proxy system modeling in high resolution paleoclimatology. *Quaternary Science Reviews*, **76**, 16–28.

Evensen, G., 1994: Sequential data assimilation with a nonlinear quasi-geostrophic model using Monte Carlo methods to forecast error statistics. *Journal of Geophysical Research: Oceans*, **99 (C5)**, 10 143–10 162.

Evensen, G., 2003: The ensemble Kalman filter: Theoretical formulation and practical implementation. *Ocean Dynamics*, **53 (4)**, 343–367.

Frank, D., U. Büntgen, R. Böhm, M. Maugeri, and J. Esper, 2007: Warmer early instrumental measurements versus colder reconstructed temperatures: shooting at a moving target. *Quaternary Science Reviews*, **26 (25-28)**, 3298–3310.

Frank, D., J. Esper, E. Zorita, and R. Wilson, 2010: A noodle, hockey stick, and spaghetti plate: a perspective on high-resolution paleoclimatology. *Wiley Interdisciplinary Reviews: Climate Change*, **1 (4)**, 507–516.

Franke, J., V. Valler, S. Brönnimann, R. Neukom, and F. Jaume-Santero, 2020: The importance of input data quality and quantity in climate field reconstructions – results from the assimilation of various tree-ring collections. *Climate of the Past*, **16 (3)**, 1061–1074, doi: 10.5194/cp-16-1061-2020.

Fritts, H. C., 1991: *Reconstructing large-scale climatic patterns from tree-ring data: a diagnostic analysis.* University of Arizona Press.

Gaspari, G., and S. E. Cohn, 1999: Construction of correlation functions in two and three dimensions. *Quarterly Journal of the Royal Meteorological Society*, **125 (554)**, 723–757.

Gill, E. C., B. Rajagopalan, P. Molnar, and T. M. Marchitto, 2016: Reduced-dimension reconstruction of the equatorial pacific sst and zonal wind fields over the past 10,000 years using mg/ca and alkenone records. *Paleoceanography*, **31 (7)**, 928–952.

Goosse, H., 2016: An additional step toward comprehensive paleoclimate reanalyses. *Journal of Advances in Modeling Earth Systems*, n/a–n/a, doi:10.1002/2016MS000739, URL http://dx.doi.org/10.1002/2016MS000739.

Goosse, H., 2017: Reconstructed and simulated temperature asymmetry between continents in both hemispheres over the last centuries. *Climate Dynamics*, **48 (5-6)**, 1483–1501.

Goosse, H., J. Guiot, M. E. Mann, S. Dubinkina, and Y. Sallaz-Damaz, 2012: The Medieval Climate Anomaly in Europe: Comparison of the summer and annual mean signals in two reconstructions and in simulations with data assimilation. *Global and Planetary Change*, **84**, 35–47.

Graham, N., and E. Wahl, 2011: Paleoclimate reconstruction challenge. *PAGES/CLIVAR Newsletter*, **19 (2)**, 71–72.

Guillet, S., and Coauthors, 2017: Climate response to the Samalas volcanic eruption in 1257 revealed by proxy records. *Nature Geoscience*, **10 (2)**, 123–128.

Guillot, D., B. Rajaratnam, and J. Emile-Geay, 2015: Statistical paleoclimate reconstructions via Markov random fields. *The Annals of Applied Statistics*, **9 (1)**, 324–352.

Hakim, G. J., J. Emile-Geay, E. J. Steig, D. Noone, D. M. Anderson, R. Tardif, N. Steiger, and W. A. Perkins, 2016: The Last Millennium Climate Reanalysis project: Framework and first results. *Journal of Geophysical Research: Atmospheres*, **121 (12)**, 6745–6764.

Harris, I., P. D. Jones, T. J. Osborn, and D. H. Lister, 2014: Updated high-resolution grids of monthly climatic observations–the CRU TS3.10 Dataset. *International Journal of Climatology*, **34 (3)**, 623–642.

Hegerl, G., and P. Stott, 2014: From past to future warming. *Science*, **343 (6173)**, 844–845.

Hegerl, G. C., T. J. Crowley, M. Allen, W. T. Hyde, H. N. Pollack, J. Smerdon, and E. Zorita, 2007: Detection of human influence on a new, validated 1500-year temperature reconstruction. *Journal of Climate*, **20 (4)**, 650–666.

Hegerl, G. C., T. J. Crowley, S. K. Baum, K.-Y. Kim, and W. T. Hyde, 2003: Detection of volcanic, solar and greenhouse gas signals in paleo-reconstructions of Northern Hemispheric temperature. *Geophysical Research Letters*, **30 (5)**, doi:10.1029/2002GL016635.

Hegerl, G. C., K. Hasselmann, U. Cubasch, J. F. Mitchell, E. Roeckner, R. Voss, and J. Waszkewitz, 1997: Multi-fingerprint detection and attribution analysis of greenhouse gas, greenhouse gas-plus-aerosol and solar forced climate change. *Climate Dynamics*, **13 (9)**, 613–634.

Houtekamer, P. L., and H. L. Mitchell, 2001: A sequential ensemble Kalman filter for atmospheric data assimilation. *Monthly Weather Review*, **129 (1)**, 123–137.

Hughes, M., and C. Ammann, 2009: The future of the past—an earth system framework for high resolution paleoclimatology: editorial essay. *Climatic Change*, **94 (3-4)**, 247–259.

Kaufman, D., 2014: A community-driven framework for climate reconstructions. *Eos, Transactions American Geophysical Union*, **95 (40)**, 361–362, doi:10.1002/2014eo400001.

Lavigne, F., and Coauthors, 2013: Source of the great AD 1257 mystery eruption unveiled, Samalas volcano, Rinjani Volcanic Complex, Indonesia. *Proceedings of the National Academy of Sciences*, **110 (42)**, 16 742–16 747.

Lean, J. L., and D. H. Rind, 2008: How natural and anthropogenic influences alter global and regional surface temperatures: 1889 to 2006. *Geophysical Research Letters*, **35 (18)**, doi: 10.1029/2008GL034864.

Liu, H., Z. Liu, and F. Lu, 2017: A systematic comparison of particle filter and EnKF in assimilating time-averaged observations. *Journal of Geophysical Research: Atmospheres*, **122 (24)**, 13–155.

Mann, M. E., R. S. Bradley, and M. K. Hughes, 1998: Global-scale temperature patterns and climate forcing over the past six centuries. *Nature*, **392 (6678)**, 779–787.

Mann, M. E., and S. Rutherford, 2002: Climate reconstruction using 'Pseudoproxies'. *Geophysical Research Letters*, **29 (10)**, 139–1.

Mann, M. E., and Coauthors, 2009: Global signatures and dynamical origins of the Little Ice Age and Medieval Climate Anomaly. *Science*, **326 (5957)**, 1256–1260.

Marsland, S. J., H. Haak, J. H. Jungclaus, M. Latif, and F. Röske, 2003: The Max-Planck-Institute global ocean/sea ice model with orthogonal curvilinear coordinates. *Ocean Modelling*, **5 (2)**, 91–127.

Masson-Delmotte, V., and Coauthors, 2013: Information from Paleoclimate Archives. *Climate Change 2013: The Physical Science Basis. Contribution of Working Group I to the Fifth Assessment Report of the Intergovernmental Panel on Climate Change*, T. F. Stocker, D. Qin, G.-K. Plattner, M. Tignor, S. Allen, J. Boschung, A. Nauels, Y. Xia, V. Bex, and P. Midgley, Eds., Cambridge University Press, Cambridge, United Kingdom and New York, NY, USA, 383–464.

Matsikaris, A., M. Widmann, and J. H. Jungclaus, 2015: On-line and off-line data assimilation in palaeoclimatology: a case study. *Climate of the Past*, **11**, 81–93.

McCarroll, D., E. Pettigrew, A. Luckman, F. Guibal, and J.-L. Edouard, 2002: Blue reflectance provides a surrogate for latewood density of high-latitude pine tree rings. *Arctic, Antarctic, and Alpine Research*, **34 (4)**, 450–453.

Meehl, G. A., W. M. Washington, C. M. Ammann, J. M. Arblaster, T. Wigley, and C. Tebaldi, 2004: Combinations of natural and anthropogenic forcings in twentieth-century climate. *Journal of Climate*, **17 (19)**, 3721–3727.

Meko, D., 1997: Dendroclimatic reconstruction with time varying predictor subsets of tree indices. *Journal of Climate*, **10**, 687–696.

Neukom, R., N. Steiger, J. J. Gómez-Navarro, J. Wang, and J. P. Werner, 2019: No evidence for globally coherent warm and cold periods over the preindustrial Common Era. *Nature*, **571 (7766)**, 550–554.

Okazaki, A., and K. Yoshimura, 2017: Development and evaluation of a system of proxy data assimilation for paleoclimate reconstruction. *Climate of the Past*, **13 (4)**, 379–393.

Oke, P. R., J. S. Allen, R. N. Miller, G. D. Egbert, and P. M. Kosro, 2002: Assimilation of surface velocity data into a primitive equation coastal ocean model. *Journal of Geophysical Research: Oceans*, **107 (C9)**, doi:10.1029/2000JC000511.

Otto-Bliesner, B. L., and Coauthors, 2016: Climate variability and change since 850 CE: An ensemble approach with the Community Earth System Model. *Bulletin of the American Meteorological Society*, **97 (5)**, 735–754.

PAGES2k Consortium, 2013: Continental-scale temperature variability during the past two millennia. *Nature Geoscience*, **6 (5)**, 339–346.

PAGES2k Consortium, 2017: A global multiproxy database for temperature reconstructions of the Common Era. *Scientific Data*, **4**, 170 088.

Parker, D., 1994: Effects of changing exposure of thermometers at land stations. *International Journal of Climatology*, **14 (1)**, 1–31.

Perkins, W. A., and G. J. Hakim, 2017: Reconstructing paleoclimate fields using online data assimilation with a linear inverse model. *Climate of the Past*, **13 (5)**, 421–436.

Phipps, S. J., and Coauthors, 2013: Paleoclimate data–model comparison and the role of climate forcings over the past 1500 years. *Journal of Climate*, **26 (18)**, 6915–6936.

Robock, A., 2000: Volcanic eruptions and climate. *Reviews of geophysics*, **38 (2)**, 191–219.

Rohde, R., and Coauthors, 2013: Berkeley Earth temperature averaging process. *Geoinformatics and Geostatistics: An Overview*, **1 (2)**, 20–100.

Rutherford, S., M. Mann, T. Delworth, and R. Stouffer, 2003: Climate field reconstruction under stationary and nonstationary forcing. *Journal of Climate*, **16 (3)**, 462–479.

Rydval, M., L.-Å. Larsson, L. McGlynn, B. E. Gunnarson, N. J. Loader, G. H. Young, and R. Wilson, 2014: Blue intensity for dendroclimatology: should we have the blues? Experiments from Scotland. *Dendrochronologia*, **32 (3)**, 191–204.

Schneider, D. P., C. M. Ammann, B. L. Otto-Bliesner, and D. S. Kaufman, 2009: Climate response to large, high-latitude and low-latitude volcanic eruptions in the Community Climate System Model. *Journal of Geophysical Research: Atmospheres*, **114 (D15)**.

Schneider, T., 2001: Analysis of incomplete climate data: Estimation of mean values and covariance matrices and imputation of missing values. *Journal of Climate*, **14 (5)**, 853–871.

Schurer, A. P., G. C. Hegerl, M. E. Mann, S. F. B. Tett, and S. J. Phipps, 2013: Separating forced from chaotic climate variability over the past millennium. *Journal of Climate*, **26 (18)**, 6954–6973, doi:10.1175/jcli-d-12-00826.1.

Schweingruber, F., H. Fritts, O. Bräker, L. Drew, and E. Schär, 1978: The x-ray technique as applied to dendroclimatology. *Tree-Ring Bulletin*, **38**, 61–91.

Seager, R., N. Graham, C. Herweijer, A. L. Gordon, Y. Kushnir, and E. Cook, 2007: Blueprints for medieval hydroclimate. *Quaternary Science Reviews*, **26 (19-21)**, 2322–2336.

Sigl, M., and Coauthors, 2015: Timing and climate forcing of volcanic eruptions for the past 2,500 years. *Nature*, **523 (7562)**, 543–549.

Smerdon, J. E., 2012: Climate models as a test bed for climate reconstruction methods: pseudo-proxy experiments. *Wiley Interdisciplinary Reviews: Climate Change*, **3 (1)**, 63–77.

Smerdon, J. E., A. Kaplan, E. Zorita, J. F. González-Rouco, and M. Evans, 2011: Spatial performance of four climate field reconstruction methods targeting the Common Era. *Geophysical Research Letters*, **38 (11)**, doi:10.1029/2011GL047372.

Smerdon, J. E., and H. N. Pollack, 2016: Reconstructing Earth's surface temperature over the past 2000 years: the science behind the headlines. *Wiley Interdisciplinary Reviews: Climate Change*, **7 (5)**, 746–771.

Solomon, A., and Coauthors, 2011: Distinguishing the roles of natural and anthropogenically forced decadal climate variability: implications for prediction. *Bulletin of the American Meteorological Society*, **92 (2)**, 141–156.

Steiger, N. J., G. J. Hakim, E. J. Steig, D. S. Battisti, and G. H. Roe, 2014: Assimilation of time-averaged pseudoproxies for climate reconstruction. *Journal of Climate*, **27 (1)**, 426–441.

Steiger, N. J., and J. E. Smerdon, 2017: A pseudoproxy assessment of data assimilation for reconstructing the atmosphere–ocean dynamics of hydroclimate extremes. *Climate of the Past*, **13 (10)**, 1435–1449.

Steiger, N. J., J. E. Smerdon, E. R. Cook, and B. I. Cook, 2018: A reconstruction of global hydroclimate and dynamical variables over the common era. *Scientific Data*, **5**, doi:10.1086/sdata.2018.86.

Stenchikov, G., K. Hamilton, R. J. Stouffer, A. Robock, V. Ramaswamy, B. Santer, and H.-F. Graf, 2006: Arctic Oscillation response to volcanic eruptions in the IPCC AR4 climate models. *Journal of Geophysical Research: Atmospheres*, **111 (D7)**.

Stevens, B., and Coauthors, 2013: Atmospheric component of the MPI-M earth system model: ECHAM6. *Journal of Advances in Modeling Earth Systems*, **5 (2)**, 146–172.

Stott, P. A., N. P. Gillett, G. C. Hegerl, D. J. Karoly, D. A. Stone, X. Zhang, and F. Zwiers, 2010: Detection and attribution of climate change: a regional perspective. *Wiley Interdisciplinary Reviews: Climate Change*, **1 (2)**, 192–211.

Stott, P. A., and G. S. Jones, 2009: Variability of high latitude amplification of anthropogenic warming. *Geophysical Research Letters*, **36 (10)**, doi:10.1029/2009GL037698.

Stott, P. A., and S. F. Tett, 1998: Scale-dependent detection of climate change. *Journal of Climate*, **11 (12)**, 3282–3294.

Sundqvist, H. S., and Coauthors, 2014: Arctic Holocene proxy climate database–new approaches to assessing geochronological accuracy and encoding climate variables. *Climate of the Past*, **10**, 1605–1631, doi:10.5194/cp-10-1605-2014.

Tardif, R., and Coauthors, 2019: Last Millennium Reanalysis with an expanded proxy database and seasonal proxy modeling. *Climate of the Past*, **15 (4)**, 1251–1273.

Taylor, K. E., R. J. Stouffer, and G. A. Meehl, 2012: An overview of CMIP5 and the experiment design. *Bulletin of the American Meteorological Society*, **93 (4)**, 485–498.

Tebaldi, C., J. M. Arblaster, and R. Knutti, 2011: Mapping model agreement on future climate projections. *Geophysical Research Letters*, **38 (23)**, doi:10.1029/2011gl049863.

Tingley, M. P., P. F. Craigmile, M. Haran, B. Li, E. Mannshardt, and B. Rajaratnam, 2012: Piecing together the past: Statistical insights into paleoclimatic reconstructions. *Quaternary Science Reviews*, **35**, 1–22.

Valler, V., J. Franke, and S. Brönnimann, 2019: Impact of different estimations of the background-error covariance matrix on climate reconstructions based on data assimilation. *Climate of the Past*, **15 (4)**, 1427–1441, doi:10.5194/cp-15-1427-2019.

Van der Schrier, G., and J. Barkmeijer, 2005: Bjerknes' hypothesis on the coldness during AD 1790–1820 revisited. *Climate Dynamics*, **25 (5)**, 537–553.

Wang, J., J. Emile-Geay, D. Guillot, N. P. McKay, and B. Rajaratnam, 2015: Fragility of reconstructed temperature patterns over the common era: Implications for model evaluation. *Geophysical Research Letters*, **42 (17)**, 7162–7170.

Wang, J., J. Emile-Geay, D. Guillot, J. E. Smerdon, and B. Rajaratnam, 2014: Evaluating climate field reconstruction techniques using improved emulations of real-world conditions. *Climate of the Past*, **10 (1)**, 1–19, doi:10.5194/cp-10-1-2014.

Whitaker, J. S., and T. M. Hamill, 2002: Ensemble data assimilation without perturbed observations. *Monthly Weather Review*, **130 (7)**, 1913–1924.

Widmann, M., H. Goosse, G. van der Schrier, R. Schnur, and J. Barkmeijer, 2010: Using data assimilation to study extratropical northern hemisphere climate over the last millennium. *Climate of the Past*, **6 (5)**, 627–644, doi:10.5194/cp-6-627-2010.

Wikle, C. K., and L. M. Berliner, 2007: A Bayesian tutorial for data assimilation. *Physica D: Nonlinear Phenomena*, **230 (1-2)**, 1–16.

Wilson, R., A. Tudhope, P. Brohan, K. R. Briffa, T. J. Osborn, and S. Tett, 2006: Two-hundred-fifty years of reconstructed and modeled tropical temperatures. *J. Geophys. Res*, **111**, C10 007, doi:10.1029/2005JC003188.

Wilson, R., and Coauthors, 2016: Last millennium northern hemisphere summer temperatures from tree rings: Part I: The long term context. *Quaternary Science Reviews*, **134**, 1–18.

Wilson, R., and Coauthors, 2019: Improved dendroclimatic calibration using blue intensity in the southern Yukon. *The Holocene*, **29 (11)**, 1817–1830.

Zhu, F., J. Emile-Geay, G. J. Hakim, J. King, and K. J. Anchukaitis, 2020: Resolving the differences in the simulated and reconstructed temperature response to volcanism. *Geophysical Research Letters*, **47 (8)**, e2019GL086 908.

Zorita, E., F. González-Rouco, and S. Legutke, 2003: Testing the approach to paleoclimate reconstructions in the context of a 1000-yr control simulation with the ECHO-G coupled climate model. *Journal of Climate*, **16 (9)**, 1378–1390.

LIST OF TABLES

TABLE 1. Summary of climate models used to construct data assimilation prior ensembles. Climate models are listed along with the identifying acronym used in this study. The years of available output are provided with the experiment used to generate them. The size of the model prior generated from these years is also provided. Taylor et al. (2012) provide more details on the PMIP3 and CMIP5 experiments, and Otto-Bliesner et al. (2016) describe the LME.

Model	Acronym	Years: Experiment	Sample size (m)
BCC-CSM1-1	BCC	850-2000: past1000	1151
CCSM4	CCSM4	850-1850: past1000 1851-2005: historical	1156
CESM1.1-CAM5	CESM	850-2005: LME full-forcing	1156
CSIRO-Mk3L-1-2	CSIRO	851-1850: past1000 1851-2000: historical	1150
FGOALS-gl	FGOALS	1000-1999: past1000	1000
HadCM3	HadCM3	850-1850: past1000 1859-2000: historical	1147
IPSL-CM5A-LR	IPSL	850-1850: past1000 1851-2005: historical	1156
MIROC-ESM	MIROC	850-1849: past1000 1850-2005: historical	1156
MRI-CGCM3	MRI	850-1850: past1000 1850-2005: historical	1156

TABLE 2. Calibrated localization radii. Localization radii for individual model priors are selected using the radius search and calibration-validation procedure detailed in Appendix A1. Skill metrics are the median values obtained for the mean extratropical MJJA time series relative to BE for the set of validation periods.

Model	Localization Radius (km)	Correlation	RMSE (°C)	σ Ratio	Mean Bias (°C)
BCC	∞	0.69	0.18	1.03	0.05
CCSM4	16500	0.72	0.19	1.18	0.07
CESM	∞	0.72	0.18	1.08	0.06
CSIRO	∞	0.70	0.19	1.18	0.05
F-GOALS	∞	0.70	0.18	1.02	0.07
HadCM3	∞	0.69	0.19	1.18	0.05
IPSL	12750	0.70	0.19	1.19	0.06
MIROC	26375	0.71	0.19	1.18	0.06
MPI	27625	0.69	0.20	1.18	0.06
MRI	∞	0.71	0.17	1.01	0.05

TABLE 3. Temperature field reconstructions used to compare spatial patterns of climate response to radiative forcings in this study. We provide a reference for each CFR along with the name used in this study. We also note the maximum size of the proxy network used in each study along with the target temperature fields.

Name	Reference	Network Size	Reconstruction Target
NTREND - DA	This study	54	MJJA
NTREND - PPR	Anchukaitis et al. (2017)	54	MJJA
Guillet 2017	Guillet et al. (2017)	28	Highpass JJA
Zhu 2020	Zhu et al. (2020)	395	JJA
LMR 2.1	Tardif et al. (2019)	544	Annual (Jan. - Dec.)
Neukom (DA)	Neukom et al. (2019)	210	Annual (April - March)

Table 4. Withheld proxy verification statistics for individual models. Reported skill metrics are the median for all individual proxy comparisons over the 54 leave-one-out assimilations.

Model	Correlation	RMSE	σ Ratio	Mean Bias °C
BCC	0.53	0.98	0.42	0.12
CCSM4	0.52	0.98	0.42	0.06
CESM	0.50	1.03	0.35	0.27
CSIRO	0.54	1.01	0.31	0.13
F-GOALS	0.47	1.04	0.34	0.06
HadCM3	0.49	1.03	0.39	0.25
IPSL	0.53	1.00	0.38	0.08
MIROC	0.53	1.01	0.37	0.25
MPI	0.53	0.99	0.39	0.11
MRI	0.55	0.98	0.32	0.16

Table A1. As in Table 2, but using the RMSE optimization scheme.

Model	Localization Radius (km)	Correlation	RMSE (°C)	σ Ratio	Mean Bias (°C)
BCC	18875	0.71	0.17	0.78	0.06
CCSM4	7375	0.71	0.18	0.81	0.07
CESM	15750	0.71	0.18	0.84	0.07
CSIRO	15750	0.70	0.18	0.80	0.06
F-GOALS	19000	0.72	0.18	0.77	0.08
HadCM3	13375	0.70	0.18	0.82	0.06
IPSL	6750	0.70	0.18	0.80	0.07
MIROC	11125	0.71	0.18	0.84	0.07
MPI	10250	0.70	0.18	0.80	0.07
MRI	20250	0.71	0.17	0.78	0.06

LIST OF FIGURES

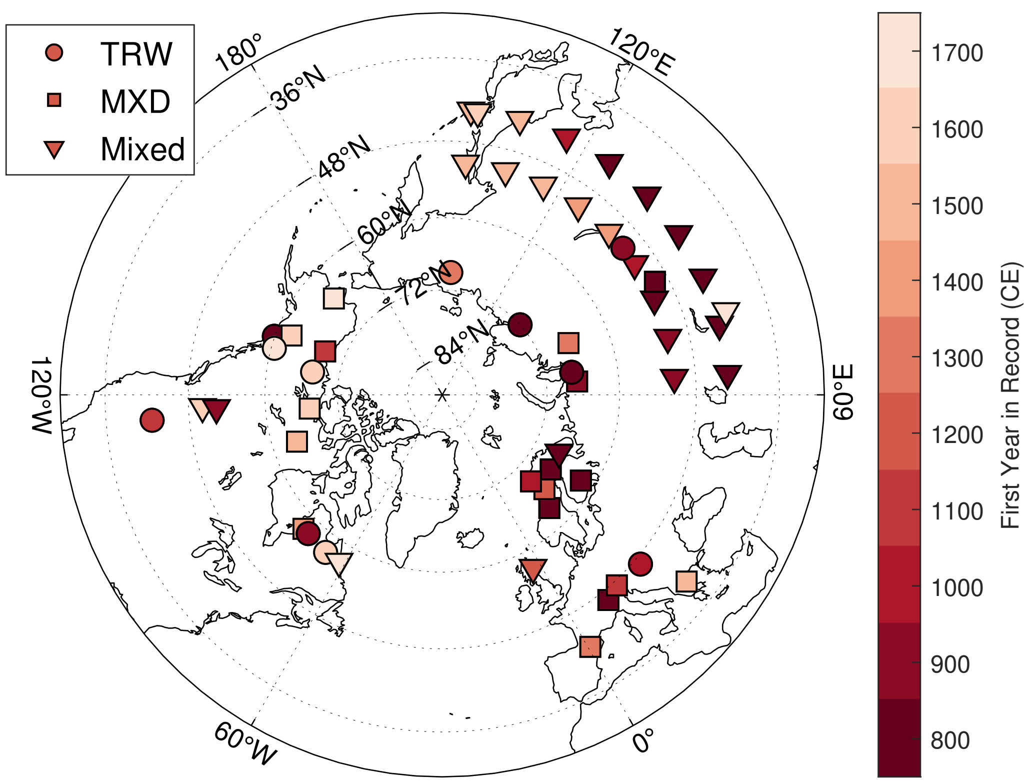

FIG. 1. Locations of the 54 NTREND sites (Wilson et al. 2016). NTREND records were developed using ring-width data (TRW; circles), maximum latewood density (MXD; squares), or a mix of TRW, MXD, and blue intensity (Mixed; triangles). Marker color denotes the century in which each record begins.

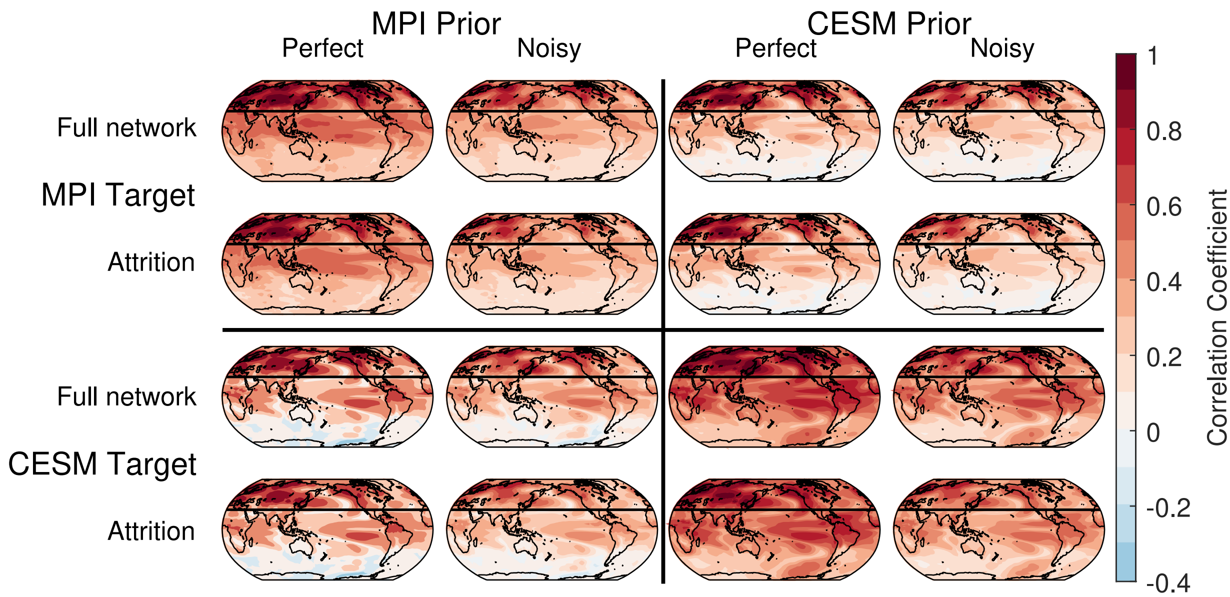

FIG. 2. Local Pearson's correlation coefficients of pseudo-proxy reconstruction temperature anomalies with the target fields. Correlation coefficients are calculated over the period 850-1988 CE. Major rows indicate the model used to generate the target field, and major columns show the model used to build the initial ensemble for each assimilation. Minor rows designate whether the proxy network exhibits no time attrition or realistic time attrition. Minor columns indicate whether reconstructions use perfect or noisy proxies. The top-left and bottom-right quadrants display the perfect-model experiments, while the top-right and bottom-left quadrants show the biased-model cases. The black line in each map indicates 30°N.

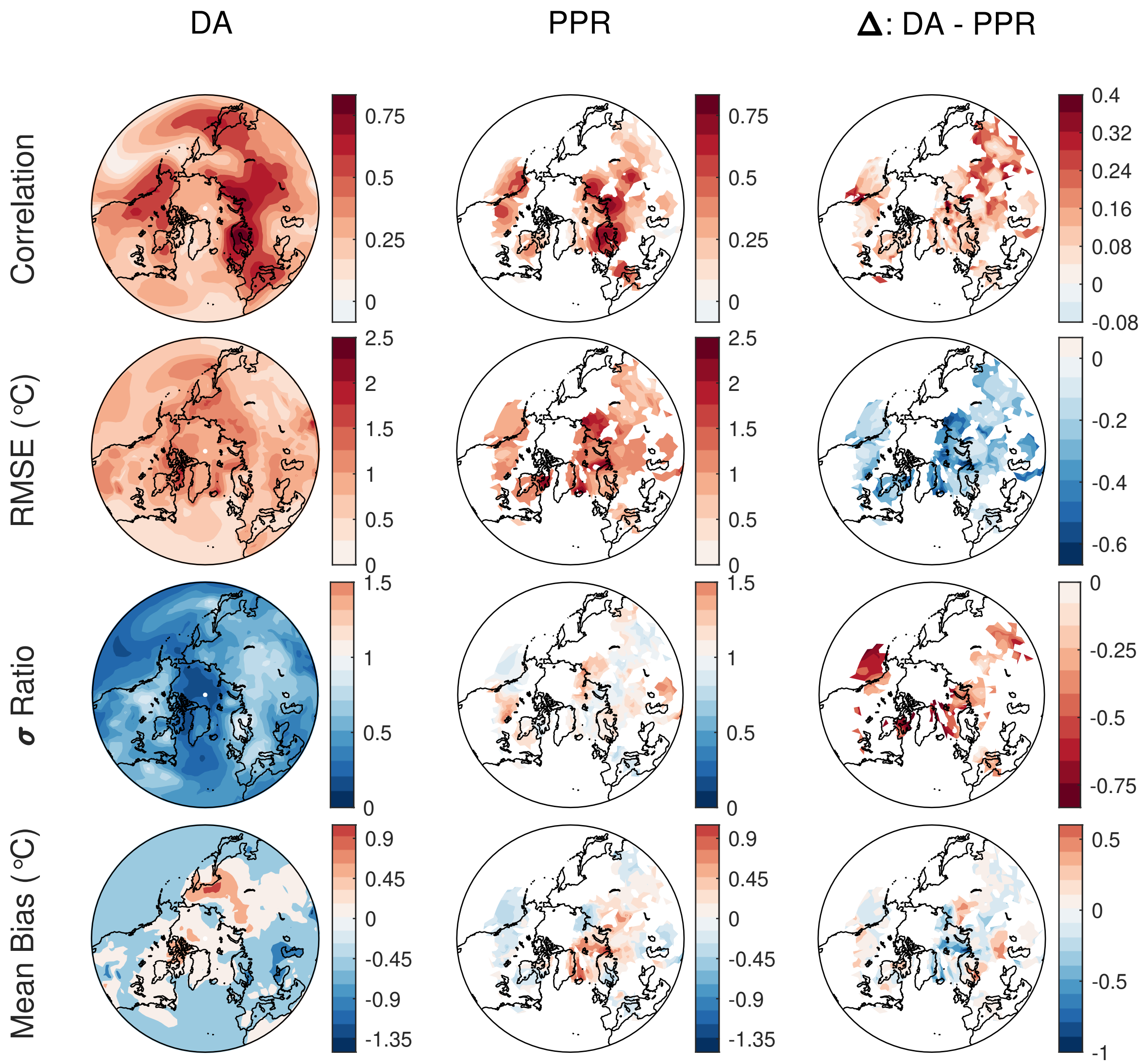

1110 FIG. 3. Pseudo-proxy reconstruction skill for DA (left column), PPR (middle), and a comparison of the two (right). Skill metrics are relative to an CESM target field using noisy proxies and realistic temporal attrition. DA results are for a biased-model MPI prior. All skill metrics are computed over the period 850-1988 CE. In order the rows detail local Pearson's correlation coefficients, RMSE values, temporal standard deviation (σ) ratios, and mean biases. Comparison plots show DA skill minus PPR skill. The comparison plot of σ ratios only considers grid points where σ is underestimated in both the DA and PPR reconstruction.

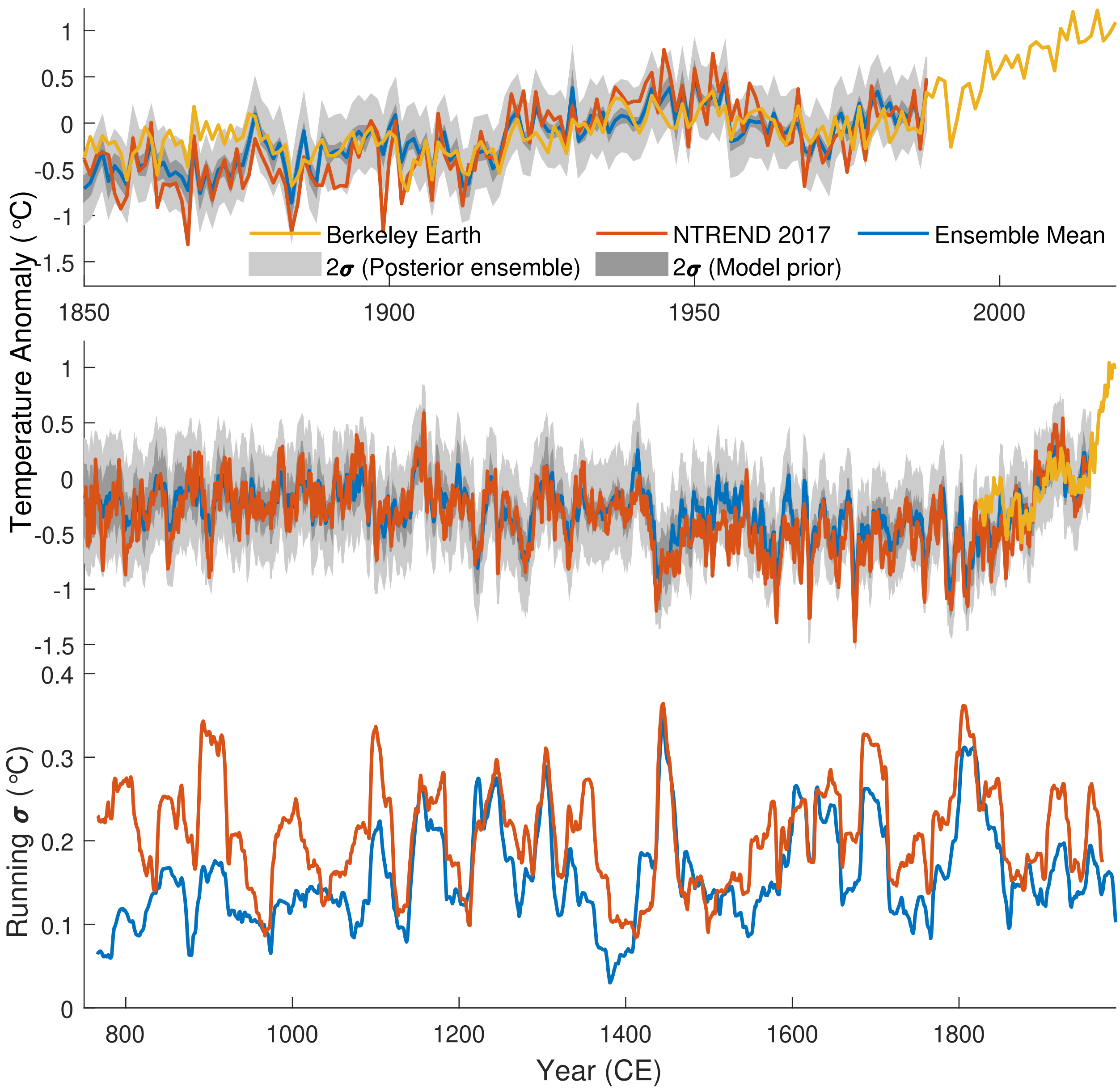

FIG. 4. Extratropical MJJA time series for the ensemble-mean reconstruction (blue), Berkeley Earth instrumental records (yellow), and Anchukaitis et al. (2017) (red). We provide two different measures of uncertainty for the DA time series: the average of the 2σ posterior ensemble width taken over the 10 reconstruction (light grey), and the 2σ width of variability arising from prior model selection (dark grey). Reconstructed temperature anomalies are shown in Celsius for the instrumental era (top), and full reconstruction (middle). A three year moving average has been applied to the time series in the middle panel. The bottom panel displays the 31-year, running standard deviation of the DA ensemble-mean and Anchukaitis et al. (2017) time series.

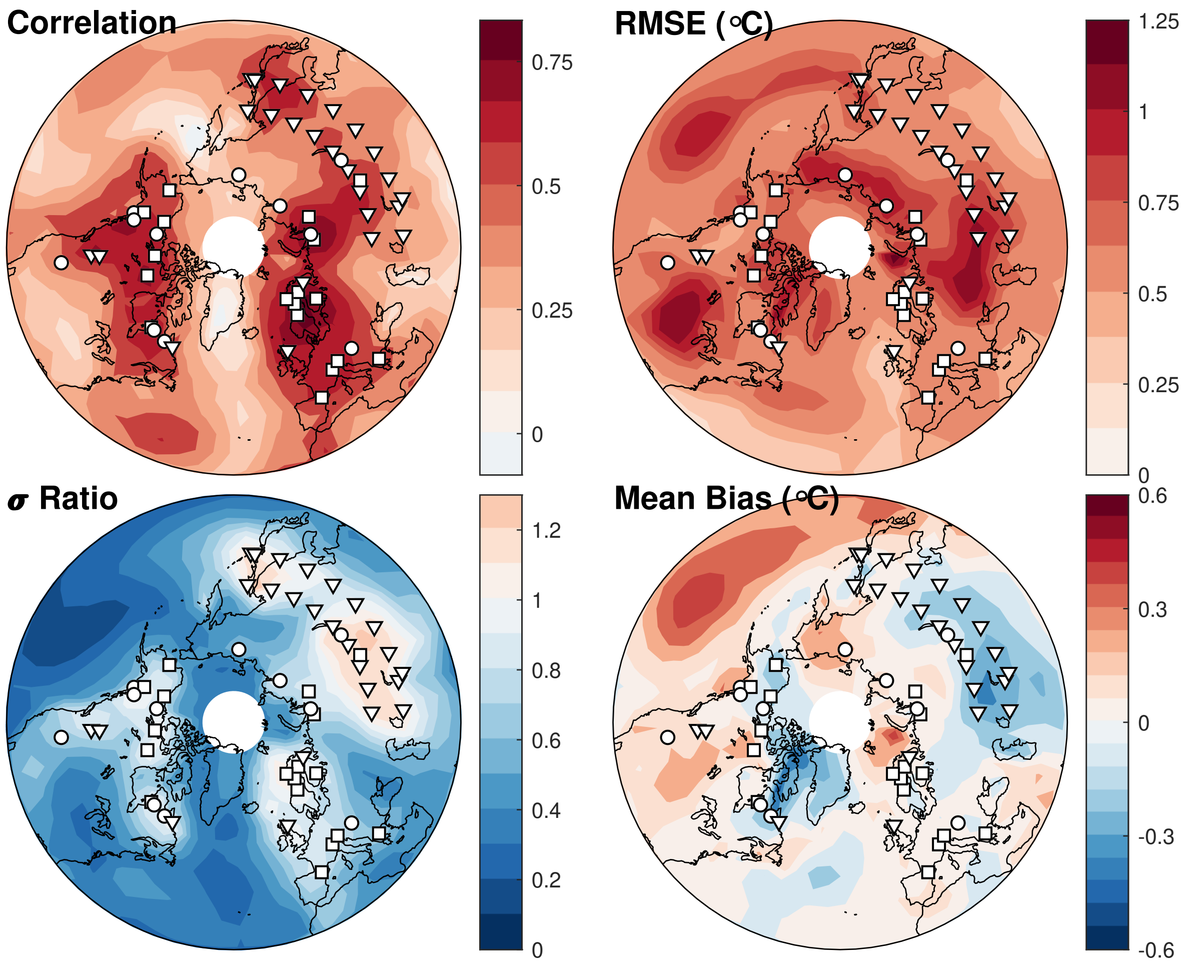

FIG. 5. Spatial skill metrics for the ensemble-mean reconstruction. Maps detail Pearson correlation coefficients (top left), RMSE values (top right), σ ratios (bottom left), and mean biases (bottom right) of reconstructed grid point time series relative to the Berkeley Earth instrumental dataset over the period 1901-1988 CE. White markers show the proxy network and marker symbols follow the convention in Figure 1.

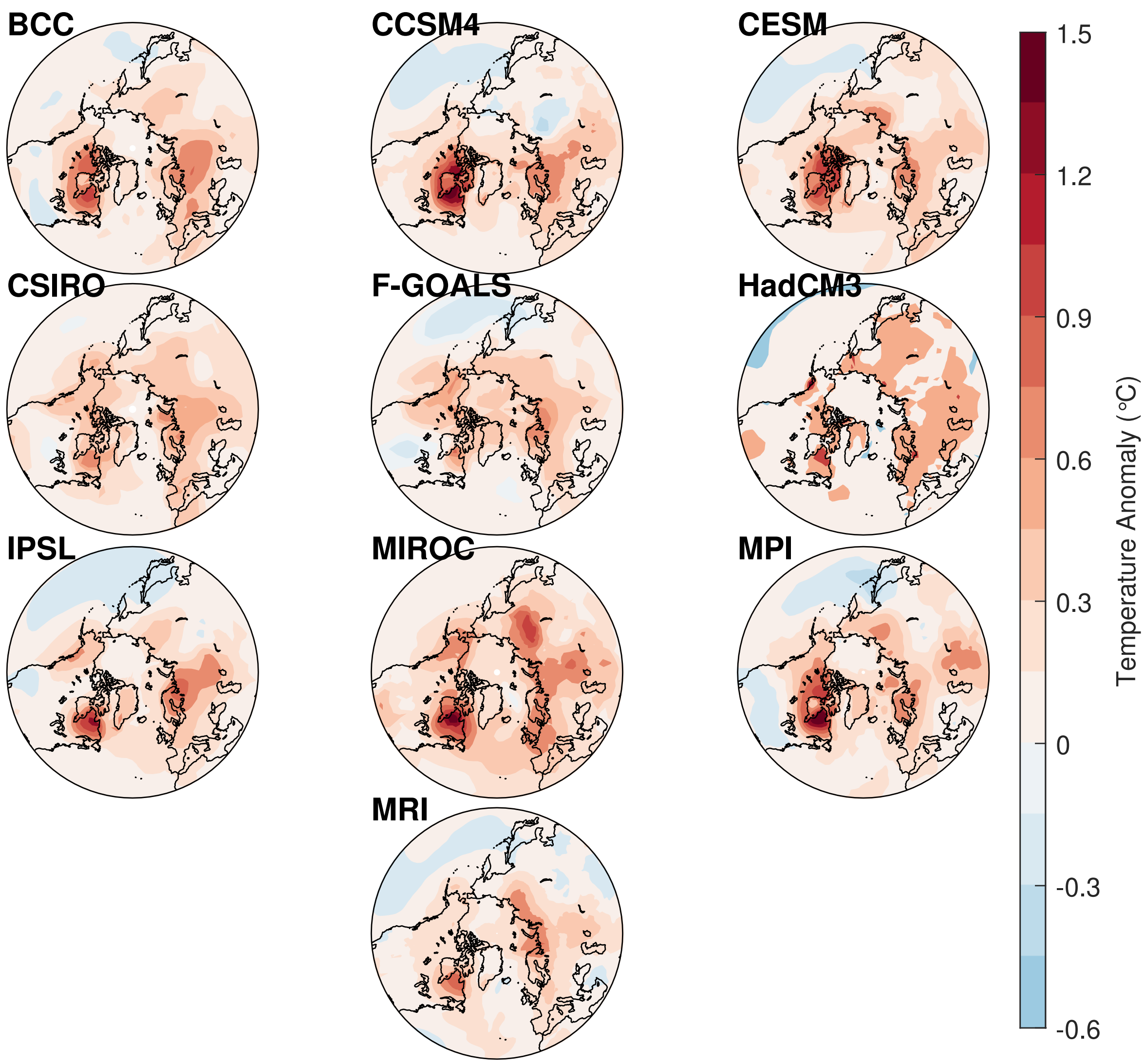

1127 Fig. 6. Reconstructed temperature anomalies (in Celsius) between the MCA (950-1250 CE) and LIA (1450-
1128 1850 CE) for the DA reconstructions. Each map shows the results for a particular model prior.

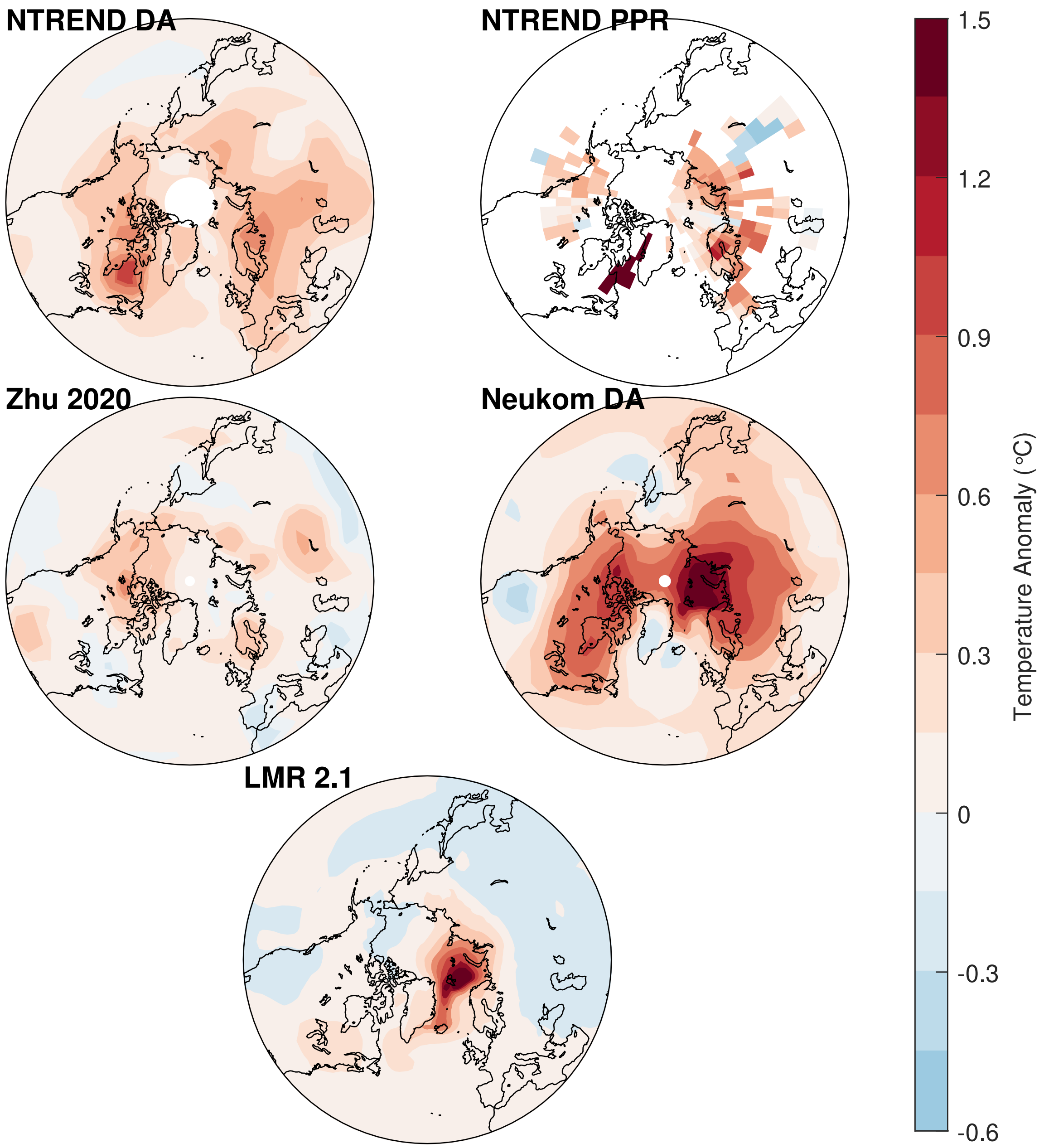

FIG. 7. As in 6, but for the temperature CFRs summarized in Table 3.

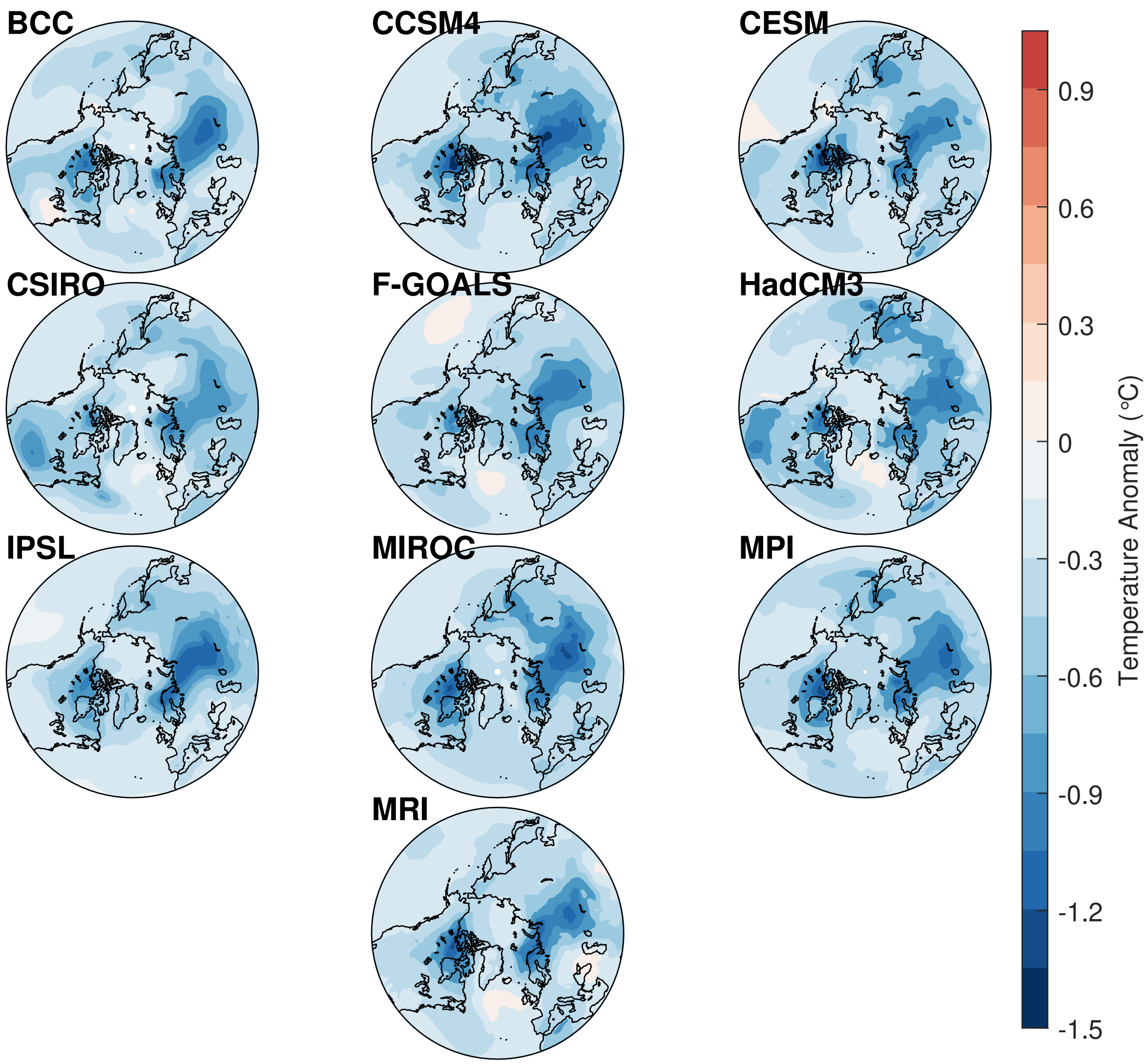

FIG. 8. Composite mean maps of the reconstructed temperature response in years containing a major tropical volcanic event. Events (N=20) are selected as tropical eruptions with a global forcing magnitude equal or larger than the 1884 Krakatoa eruption: this set consists of 916, 1108, 1171, 1191, 1230, 1258, 1276, 1286, 1345, 1453, 1458, 1595, 1601, 1641, 1695, 1809, 1815, 1832, 1836, and 1884 CE (Sigl et al. 2015; Anchukaitis et al. 2017). Temperature anomalies (in Celsius) are determined relative to the mean temperature of the five years preceding each volcanic event. Each map shows the results for a particular model prior.

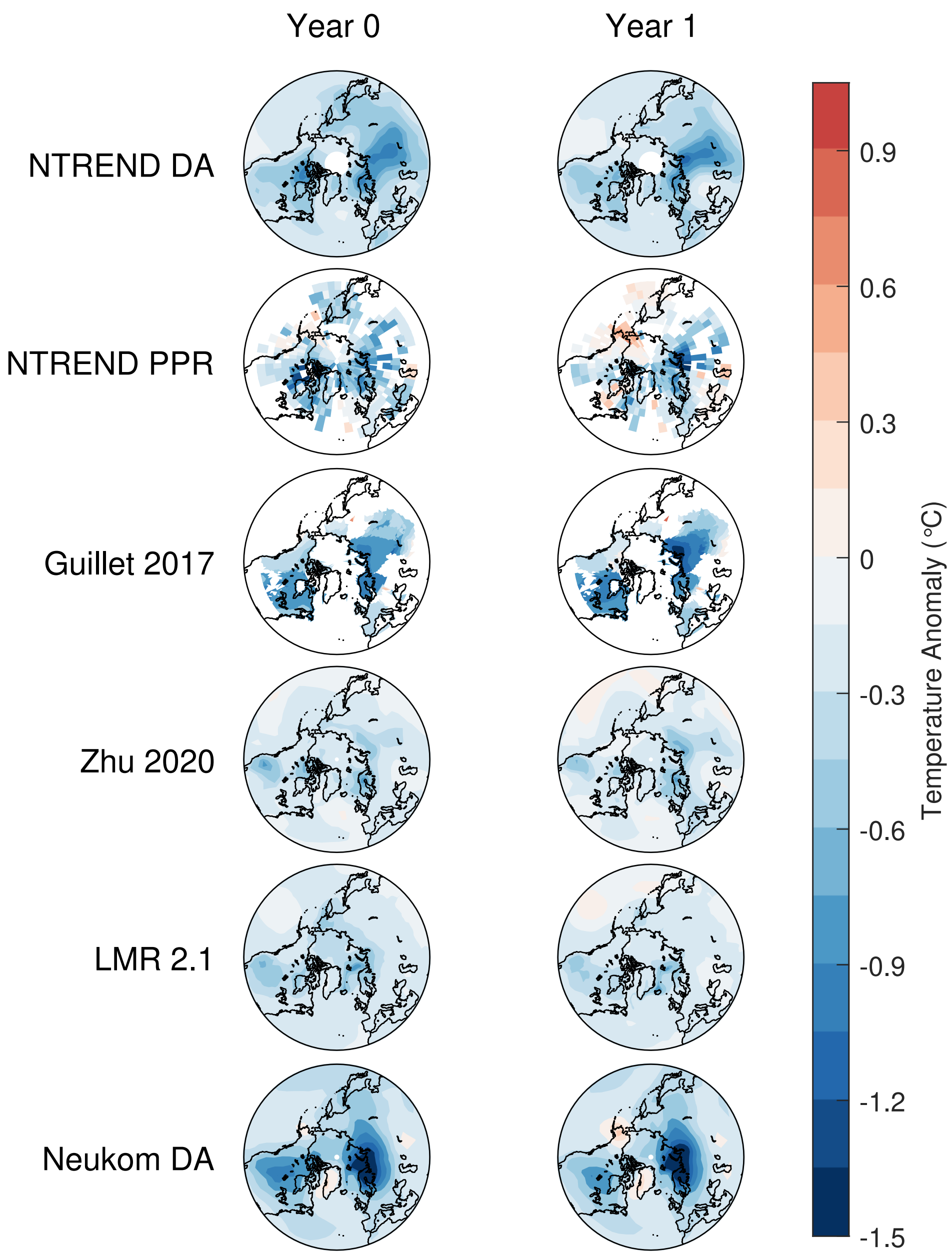

1135 FIG. 9. As in Figure 8, but for the temperature CFRs summarized in Table 3 (rows). Maps show the composite
1136 mean response in years with a major tropical eruption (left), and in the year following a major eruption (right).

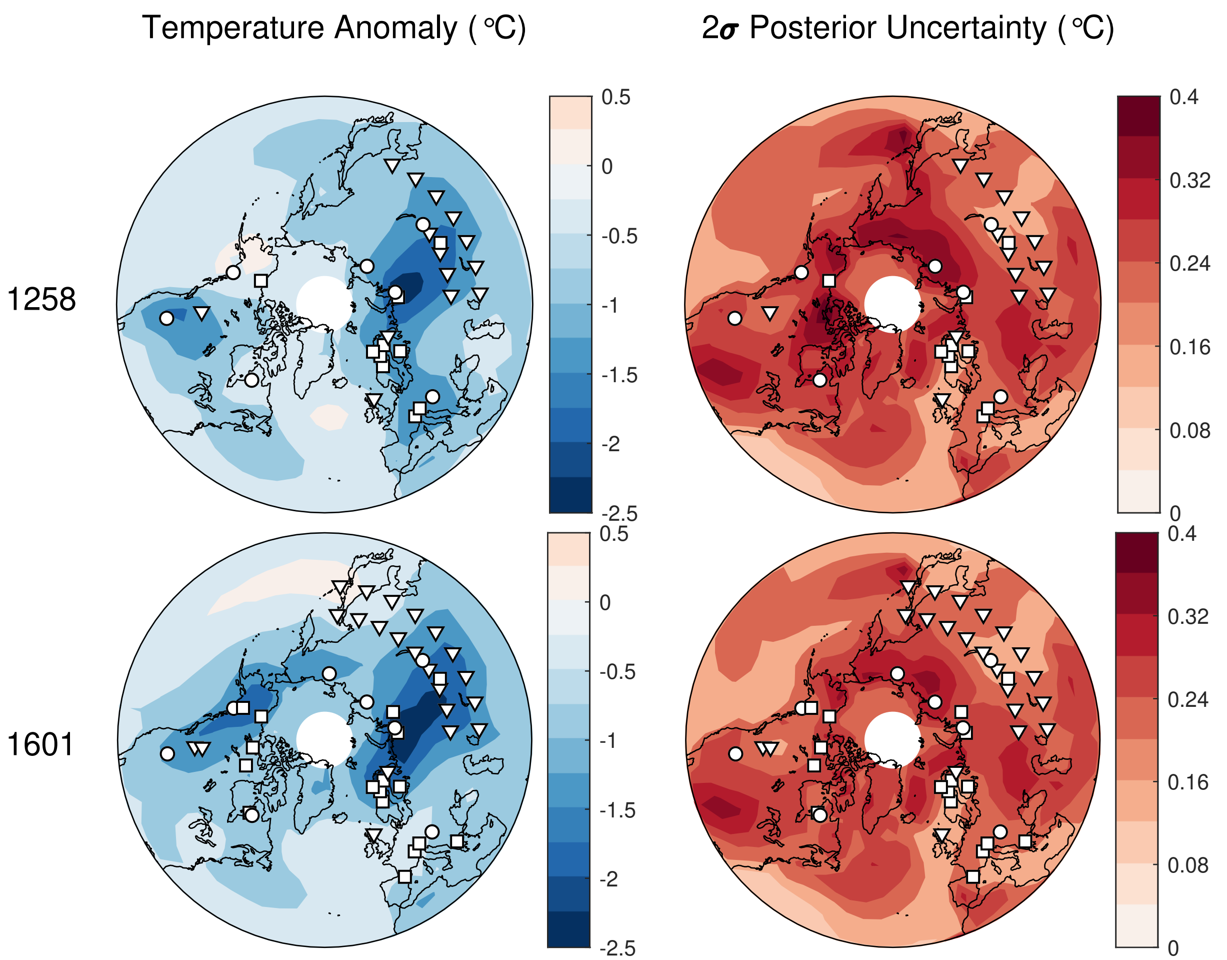

FIG. 10. Spatial characteristics in the year following volcanic eruptions in 1257 (top) and 1600 (bottom) (De Silva and Zielinski 1998; Lavigne et al. 2013) in the ensemble-mean reconstruction. The left side displays temperature anomalies relative to the five preceding years in Celsius. The right side shows the average 2σ width of the posterior ensembles averaged across the 10 reconstructions. White markers show the proxy network for each event. Marker symbols follow the convention in Figure 1.